

ISO observations of obscured Asymptotic Giant Branch stars in the Large Magellanic Cloud^{*}

N.R. Trams¹, J.Th. van Loon², L.B.F.M. Waters^{2,3}, A.A. Zijlstra⁴, C. Loup⁵, P.A. Whitelock⁶, M.A.T. Groenewegen⁷, J.A.D.L. Blommaert⁸, R. Siebenmorgen⁸, A. Heske⁸, and M.W. Feast⁹

¹ Integral Science Operations Centre, Astrophysics Div., Science Department, ESTEC, P.O.Box 299, 2200 AG Noordwijk, The Netherlands

² Astronomical Institute, University of Amsterdam, Kruislaan 403, 1098 SJ Amsterdam, The Netherlands

³ Space Research Organization Netherlands, Landleven 12, 9700 AV Groningen, The Netherlands

⁴ University of Manchester Institute of Science and Technology, P.O.Box 88, Manchester M60 1QD, UK

⁵ Institut d'Astrophysique de Paris, 98bis Boulevard Arago, F-75014 Paris, France

⁶ South African Astronomical Observatory, P.O. Box 9, 7935 Observatory, South Africa

⁷ Max-Planck-Institut für Astrophysik, Karl-Schwarzschild-Strasse 1, D-85740 Garching bei München, Germany

⁸ ISO Data Centre, Astrophysics Division, Science Department of ESA, Villafranca del Castillo, P.O. Box 50727, E-28080 Madrid, Spain

⁹ Astronomy Department, University of Cape Town, 7700 Rondebosch, South Africa

Received 2 February 1999 / Accepted 9 April 1999

Abstract. We present ISO photometric and spectroscopic observations of a sample of 57 bright Asymptotic Giant Branch stars and red supergiants in the Large Magellanic Cloud, selected on the basis of IRAS colours indicative of high mass-loss rates. PHOT-P and PHOT-C photometry at 12, 25 and 60 μm and CAM photometry at 12 μm are used in combination with quasi-simultaneous ground-based near-IR photometry to construct colour-colour diagrams for all stars in our sample. PHOT-S and CAM-CVF spectra in the 3 to 14 μm region are presented for 23 stars. From the colour-colour diagrams and the spectra, we establish the chemical types of the dust around 49 stars in this sample. Many stars have carbon-rich dust. The most luminous carbon star in the Magellanic Clouds has also a (minor) oxygen-rich component. OH/IR stars have silicate absorption with emission wings. The unique dataset presented here allows a detailed study of a representative sample of thermal-pulsing AGB stars with well-determined luminosities.

Key words: stars: carbon – stars: circumstellar matter – stars: mass-loss – stars: AGB and post-AGB – galaxies: Magellanic Clouds – infrared: stars

1. Introduction

One of the least expected achievements of the Infra-Red Astronomical Satellite (IRAS; Neugebauer et al. 1984) was the detection of a large number of mid-IR point sources in the Large Magellanic Cloud (LMC) just above its limits of sensitivity (IRAS

Point Source Catalogue; Schwering & Israel 1990). Many of these are candidates for intermediate-mass stars at the tip of the Asymptotic Giant Branch (AGB). Their lives drawing to a close, these stars are shedding their stellar mantles at rates of up to $10^{-4} M_{\odot} \text{ yr}^{-1}$. Their dusty circumstellar envelopes (CSEs) obscure the optical light from the star and become very bright IR objects. The details of the evolution and mass loss of AGB stars are poorly understood. The study of galactic samples of AGB stars is severely hampered by the difficulty to determine accurate distances to stars in the Milky Way. The distance to the LMC, however, is well known and hence luminosities and mass-loss rates of AGB stars in the LMC may be determined with a high degree of accuracy.

Early explorations of the IRAS data in combination with ground-based near-IR observations resulted in the first identifications of mid-IR sources in the LMC with obscured AGB stars (Reid et al. 1990; Wood et al. 1992). We have successfully increased the sample of known AGB counterparts of IRAS sources in the LMC from a dozen to more than 50 stars (Loup et al. 1997; Zijlstra et al. 1996; van Loon et al. 1997, 1998a: Papers I to IV). We attempted to classify their photospheres and CSEs as oxygen- or carbon-dominated, but for the majority of the stars this could not be done conclusively. There remained therefore considerable uncertainty about the luminosity distribution of the obscured carbon stars. This information is important for testing current understanding of the evolution of AGB stars, including dredge-up of carbon and nuclear burning at the bottom of the convective mantle (Hot Bottom Burning, HBB).

57 obscured AGB stars and a few red supergiants (RSGs) in the LMC were selected for Guaranteed Time and follow-up Open Time observations with the Infrared Space Observatory (ISO; Kessler et al. 1996). The goals were to obtain photometry at 12, 25 and 60 μm and to spectroscopically determine the chemical types of the CSEs. The photometry, which covers the

Send offprint requests to: N.R. Trams (ntrams@astro.estec.esa.nl)

^{*} This paper is based on observations with the Infrared Space Observatory (ISO). ISO is an ESA project with instruments funded by ESA member states (especially the PI countries: France, Germany, The Netherlands and the United Kingdom) and with the participation of ISAS and NASA.

Table 1. IRAS detected stars observed with ISO: names (LI stands for LI-LMC (Schwering & Israel 1990), TRM is from Reid et al. (1990), HV is from Payne-Gaposchkin (1971), SP is from Sanduleak & Philip (1977) and WOH is from Westerlund et al. (1981); sources will be referenced hereafter by their bold-faced names), ISO pointing coordinates (J2000), and references: 1: Hodge & Wright (1969); 2: Eggen (1971); 3: Wright & Hodge (1971); 4: Dachs (1972); 5: Sandage & Tammann (1974); 6: Glass (1979); 7: Humphreys (1979); 8: Blanco et al. (1980); 9: Feast et al. (1980); 10: Bessell & Wood (1983); 11: Wood et al. (1983); 12: Rebeiro et al. (1983); 13: Prevot et al. (1985); 14: Elias et al. (1985); 15: Wood et al. (1985); 16: Elias et al. (1986); 17: Wood et al. (1986); 18: Reid et al. (1988); 19: Reid (1989); 20: Hughes (1989); 21: Hughes & Wood (1990); 22: Reid et al. (1990); 23: Hughes et al. (1991); 24: Wood et al. (1992); 25: Roche et al. (1993); 26: Groenewegen et al. (1995); 27: Zijlstra et al. (1996); 28: Ritossa et al. (1996); 29: van Loon et al. (1996); 30: van Loon et al. (1997); 31: Loup et al. (1997); 32: Oestreicher et al. (1997); 33: van Loon et al. (1998a); 34: Groenewegen & Blommaert (1998); 35: van Loon et al. (1998b); 36: van Loon et al. (1999)

LI	IRAS	TRM	HV	RA (2000)	Decl (2000)	Other names	References
<i>IRAS detected stars</i>							
1825	04286–6937	–	–	04 28 30.3	–69 30 49	–	27,31,33
1844	04374–6831	–	–	04 37 22.8	–68 25 03	–	27,31,33
4	04407–7000	–	–	04 40 28.4	–69 55 13	–	27,31,33
57	04496–6958	–	–	04 49 18.6	–69 53 14	–	27,31,33,34,36
60	04498–6842	–	–	04 49 41.4	–68 37 50	–	27,31,33,36
77	04509–6922	–	–	04 50 40.2	–69 17 33	–	24,27,28,33,36
92	04516–6902	–	–	04 51 28.4	–68 57 53	–	24,27,33
121	04530–6916	–	–	04 52 45.3	–69 11 53	–	24,27,28
141	04539–6821	–	–	04 53 46.3	–68 16 12	–	27,31,33
153	04544–6849	–	–	04 54 14.4	–68 44 13	SP77 30-6 , WOH SG66	12,13,20,21,27,31
159	04545–7000	–	–	04 54 09.8	–69 56 00	–	24,27
181	04553–6825	–	–	04 55 10.1	–68 20 35	WOH G64	16,17,19,24,25,27,29,31,33,35,36
198	04557–6753	–	–	04 55 38.9	–67 49 10	–	27,31,33
203	04559–6931	–	12501	04 55 41.6	–69 26 25	SP77 31-20, WOH SG097	11,12,13,20,22,27,32,33
297	05003–6712	–	–	05 00 18.9	–67 08 02	–	27,30,31,33,36
310	05009–6616	–	–	05 01 03.8	–66 12 40	–	27,31,33,36
383	05042–6720	48	888	05 04 14.3	–67 16 17	SP77 29-33, WOH SG140	5,6,7,11,14,18,22,31,32
570	05112–6755	4	–	05 11 10.1	–67 52 17	–	22,27,31,33,36
571	05113–6739	24	–	05 11 13.7	–67 36 35	–	22,27,31,33
578	–	72	–	05 11 41.2	–66 51 12	–	22,27,31,33
612	05128–6728	43	2360	05 12 46.4	–67 19 37	SP77 37-24, WOH SG193	3,5,6,7,11,14,18,22,31
1880	05128–6455	–	–	05 13 04.6	–64 51 40	–	27,31,33,36
663	05148–6730	36	916	05 14 49.9	–67 27 19	SP77 37-35, WOH SG204	1,2,4,6,7,11,18,22,31,32
793	05190–6748	20	–	05 18 56.7	–67 45 06	–	22,27,31,33
–	–	88	–	05 20 20.9	–66 36 00	–	22,27,31,33,34,36
–	–	45	–	05 28 16.3	–67 20 55	–	22,27,31,33
1157	05295–7121	–	–	05 28 40.8	–71 19 13	–	27,31
1130	05289–6617	99	–	05 29 02.6	–66 15 31	–	22,27,31
1145	–	–	5870	05 29 03.5	–69 06 47	SP77 47-17, WOH SG331	9,11,20,31
1153	05294–7104	–	–	05 28 47.8	–71 02 29	–	24,27,31
1164	05298–6957	–	–	05 29 24.5	–69 55 14	–	24,27,31,36
1177	05300–6651	79	–	05 30 04.2	–66 49 23	–	22,27,31,36
1238	05316–6604	101	–	05 31 45.9	–66 03 51	WOH SG374	22,27,31
1281	05327–6757	5	996	05 32 36.0	–67 55 08	SP77 46-59, WOH SG388	7,11,17,18,22,31
1286	05329–6708	60	–	05 32 52.5	–67 06 25	–	17,22,24,26,27,31,33,36
1345	05348–7024	–	–	05 34 16.1	–70 22 53	–	27,31,33
1382	05360–6648	77	–	05 36 03.3	–66 46 47	–	22,27,31,33
1506	05402–6956	–	–	05 39 44.6	–69 55 18	–	24,27
1756	05506–7053	–	–	05 50 09.1	–70 53 12	–	27,31,33
1790	05558–7000	–	–	05 55 20.8	–70 00 05	–	27,31
1795	05568–6753	–	–	05 56 38.7	–67 53 39	–	27,31

entire spectral energy distributions (SEDs), can be modelled and used to derive accurate luminosities and mass-loss rates. In this paper we present the ISO data and classify sources as oxygen- or carbon-rich.

2. Source selection

The sources observed with ISO were selected from the lists presented in Paper I, where all IRAS candidate AGB stars in the MCs are listed. We selected 30 infrared AGB stars or RSGs

Table 2. The list of program stars without IRAS counterpart. The references are as in Table 1. SHV is from Hughes (1989), BMB is from Blanco et al. (1980), WBP is from Wood et al. (1985) and GRV is from Reid et al. (1988).

LI	IRAS	TRM	HV	RA (2000)	Decl (2000)	Other names	References
<i>non-IRAS sources classified as C stars</i>							
–	–	–	–	04 53 59.7	–67 45 47	SHV0454030–675031	20,21
–	–	–	–	05 02 28.7	–69 20 10	SHV0502469–692418	20,21,23
–	–	–	2379	05 14 46.3	–67 55 47	–	3,10,11,20
–	–	–	–	05 20 46.8	–69 01 25	SHV0521050–690415 , BCB-R046	8,20,21,23
–	–	–	–	05 25 30.6	–70 09 13	SHV0526001–701142	20,21
–	–	–	–	05 26 17.4	–69 08 07	WBP14	15
–	–	–	–	05 35 11.4	–70 22 46	SHV0535442–702433	20,21
<i>non-IRAS sources classified as M or S stars</i>							
–	–	–	2446	05 20 01.5	–67 34 43	WOH G274, GRV0520–6737	11,18
–	–	–	–	05 21 33.1	–70 09 56	SHV0522023–701242	20,21
–	–	–	–	05 21 40.5	–70 22 31	SHV0522118–702517	20,21
–	–	–	–	05 24 31.3	–69 43 25	SHV0524565–694559	20,21
–	–	–	–	05 30 00.3	–70 20 06	SHV0530323–702216	20,21,23
–	–	–	12070	05 52 27.8	–69 14 12	WOH SG515	9,11
<i>non-IRAS sources without spectral classification</i>							
–	–	–	–	05 00 11.2	–68 12 48	SHV0500193–681706	20,21
–	–	–	–	05 00 13.5	–68 24 56	SHV0500233–682914	20,21
–	–	–	–	05 19 41.8	–66 57 50	GRV0519–6700	18

without optical counterparts from their Table 2. These objects should represent the brightest, most obscured AGB stars. Four objects from this table were excluded because of their red IRAS colours ($S_{25}/S_{12} \gtrsim 2.5$): LI-LMC528, 861, 1137 and 1341. We also selected 8 sources from the optically known M and C stars with IRAS counterparts in Table 1 of Paper I. These include well known Harvard Variables as well as the optically thick source IRAS04553–6825 (LI-LMC181, WOH G64; Elias et al. 1986; Wood et al. 1986). Two unidentified IRAS sources from Table 4 of Paper I have been included in the present sample. LI-LMC203 is near an M1.5 star (HV12501), but there is also an A3 Iab supergiant (Sk–69-39a) close to the IRAS position. For LI-LMC1795 we found a bright R-band counterpart (Paper II). Finally one source from Table 7 of Paper I was included (LI-LMC1130). Although listed in Paper I as a foreground star, it was included here in an attempt to establish whether this is true. For these last three stars the higher spatial resolution ISO observations at 12 μm allow a better identification of the source with one of the possible counterparts found near the IRAS position. The 41 IRAS sources included in this study are listed in Table 1, with the most common names for these objects, their coordinates (J2000) and some references. The coordinates for the pointings of the ISO observations were taken from the SIMBAD astronomical database in 1994.

The selection of IRAS detected AGB stars gives a sample that is severely biased towards very luminous stars (including supergiants). We therefore also included 16 non-IRAS stars. These were mostly taken from Wood et al. (1983, 1985), Reid et al. (1990) and Hughes (1989). Seven of these objects are classified as C stars from optical spectra or near-IR colours. Six objects are classified as M or S stars and for three objects

no classification is available. This group of non-IRAS sources also includes the RCB-like variable HV2379 (Bessell & Wood 1983). These sources are listed in Table 2.

3. IRAS data

Here the IRAS data are discussed, for later comparison with the ISO photometry. Data at 12, 25, 60 and 100 μm was retrieved from the IRAS data base server in Groningen¹ (Assendorp et al. 1995). The Groningen Gipsy data analysis software was used to measure the flux density from a trace through the position of the star (Gipsy command SCANAID). For the 60 and 100 μm data, 2×2 square degree maps were created with 0.5' pixels to find point sources coincident with the positions of the stars. The 12 and 25 μm flux densities have a 1- σ error of a few per cent, with a minimum error of ~ 0.01 Jy. The 60 and 100 μm flux densities are much less certain, and it is also more difficult to assess reliable error estimates: 10% would be a typical error. The faintest 60 μm sources that IRAS detected were assigned $F_{60} = 0.1$ Jy. Only one source was well detected at 100 μm . The flux densities are listed in Table 3. When it is not certain that the measured flux density is physically related to the star of interest it is marked with a colon.

All of our sources that are in the IRAS-PSC, plus HV5870 (=LI-LMC1145) and TRM72 (=LI-LMC578) that are in Schw-

¹ The IRAS data base server of the Space Research Organisation of the Netherlands (SRON) and the Dutch Expertise Centre for Astronomical Data Processing is funded by the Netherlands Organisation for Scientific Research (NWO). The IRAS data base server project was also partly funded through the Air Force Office of Scientific Research, grants AFOSR 86-0140 and AFOSR 89-0320.

Table 3. Revised IRAS 12, 25, 60 and 100 μm photometry (in Jy), accompanied by a colon if questionable.

Star	F_{12}	F_{25}	F_{60}	F_{100}
GRV0519–6700	<0.06	<0.02	<0.1	
HV12070	0.06	0.03	0.1:	
HV12501	0.23	0.06	<1.0	
HV2360	0.38	0.35	0.4:	
HV2379	0.05	0.02	<0.8	
HV2446	0.05	0.02	<0.2	
HV5870	0.30	0.17	<5.0	
HV888	0.58	0.29	<4.0	
HV916	0.44	0.23	<2.0	
HV996	0.71	0.53	<0.5	
IRAS04286–6937	0.28	0.20	<0.1	
IRAS04374–6831	0.24	0.12	0.1:	
IRAS04407–7000	0.76	0.76	0.1	
IRAS04496–6958	0.31	0.19	0.1	
IRAS04498–6842	1.33	0.89	<0.2	
IRAS04509–6922	0.89	0.86	<2.0	
IRAS04516–6902	0.86	0.55	0.4:	
IRAS04530–6916	2.07	5.09	22.0	28.0
IRAS04539–6821	0.22	0.12	0.1:	
IRAS04545–7000	0.46	0.83	<0.5	
IRAS04557–6753	0.24	0.14	<0.3	
IRAS05003–6712	0.43	0.33	0.1:	
IRAS05009–6616	0.28	0.14	<0.4	
IRAS05112–6755	0.46	0.33	0.7:	
IRAS05113–6739	0.25	0.14	0.1:	
IRAS05128–6455	0.23	0.24	0.1	
IRAS05190–6748	0.39	0.25	0.1:	
IRAS05289–6617	0.16	0.39	0.3	
IRAS05294–7104	0.69	0.56	<3.0	
IRAS05295–7121	0.23	0.08	<0.3	
IRAS05298–6957	0.85	1.38	<3.0	
IRAS05300–6651	0.28	0.17	0.1:	
IRAS05329–6708	0.74	1.23	0.2:	
IRAS05348–7024	0.58	0.16	<1.0	
IRAS05360–6648	0.21	0.09	0.3:	
IRAS05402–6956	0.71	1.02	<2.0	
IRAS05506–7053	0.28	0.16	<0.2	
IRAS05558–7000	0.85	0.80	0.2:	
IRAS05568–6753	0.35	0.43	0.2	
SHV0454030–675031	<0.03	<0.03	<0.2	
SHV0500193–681706	0.11:	0.07	<0.3	
SHV0500233–682914	0.10:	0.03	<1.5	
SHV0502469–692418	0.02:	<0.03	<0.1	
SHV0521050–690415	0.06:	0.02:	<0.7	
SHV0522023–701242	<0.10	<0.04	0.4:	
SHV0522118–702517	0.06:	0.05	<2.2	
SHV0524565–694559	<0.14	<0.07	<1.0	
SHV0526001–701142	0.07:	0.01:	0.1:	
SHV0530323–702216	<0.04	<0.04	0.4	
SHV0535442–702433	0.01:	0.07:	<1.0	
SP77 30–6	0.26	0.13	0.1:	
TRM45	0.07	0.07	<2.0	
TRM72	0.22	0.06	<0.3	
TRM88	0.17	0.04	<0.7	
WBP14	0.01:	<0.03	<4.0	
WOH G64	8.45	13.53	2.2	
WOH SG374	0.37	0.38	0.2:	

ering & Israel (1990), were recovered with good flux density determinations at 12 μm . Reliable 12 μm flux densities could also be determined for IRAS05128–6455 and 05289–6617, below their upper limits as listed in the PSC. Neither in the PSC, nor in Schwering & Israel (1990), are HV12070, HV2379, HV2446, TRM45, and TRM88 secure detections. Detection is not certain for WBP14 and the SHV sources for which flux density estimates are listed. The 12 μm flux densities of the GRV source and four SHV sources are upper limits. IRAS05506–7053 looks extended or multiple.

At 25 μm detections seem a little more reliable than at 12 μm , at a given flux density. Rather surprisingly, the detection limit at 25 μm is at least as faint as at 12 μm ; sources with $F_{25} \sim 0.02$ Jy could be found (see also Reid et al. 1990). This is, however, only possible because the positions of the stars are known. For SP77 30–6 and all eight (other) IRAS sources the PSC lists only upper limits of $F_{25} < 0.25$ Jy. SHV0502469–692418 and WBP14 were the only sources that were (tentatively) detected at 12 μm but not at 25 μm . Their flux densities are probably below the limit of detection, $F_{25} < 0.01$ Jy, if their colours are rather blue.

At 60 μm , IRAS05298–6957 is a bright, small but extended source about 10' in diameter, with $F_{60} \sim 2$ Jy. No point source could be distinguished on top of this emission, that is probably associated with the small cluster of which IRAS05298–6957 is a member (Paper IV). Flux densities are listed for two dozen sources, but it is not sure how many among these are real detections and how many are spurious. The only 60 μm detections in the PSC are IRAS04516–6902 (0.80 ± 0.19 Jy), 04530–6916 (20.51 ± 1.85 Jy) and 05112–6755 (0.91 ± 0.11 Jy), all consistent with our estimates. More stringent upper limits are put on the 60 μm flux densities of the other sources.

At 100 μm sources may be detected as faint as a few Jy. The only detection, however, is the brightest far-IR source in our sample, IRAS04530–6916, which we measured at $F_{100} = 28$ Jy. This is consistent with the PSC upper limit of 46.17 Jy.

The new flux density estimates can be compared with the literature values from the PSC or Schwering & Israel (1990) (Fig. 1). On average, the new flux densities are only a few per cent fainter than the values from the literature. Flux densities $F_{25} \lesssim 0.2$ Jy may have been over-estimated in the past. HV12501 with $F_{\text{rev}}/F_{\text{lit}} = 0.56$ and 0.32 at 12 and 25 μm , respectively, and IRAS05506–7053 with $F_{\text{rev}}/F_{\text{lit}} = 0.67$ and 0.42 at 12 and 25 μm , respectively, are the most extreme examples of this. Schwering & Israel (1990) over-estimated the 25 μm flux density of TRM72 ($F_{\text{rev}}/F_{\text{lit}} = 0.55$), but under-estimated the 12 μm flux density of HV5870 ($F_{\text{rev}}/F_{\text{lit}} = 2.00$). The other two flux densities which are obviously under-estimated are for SP77 30–6 at 12 μm ($F_{\text{rev}}/F_{\text{lit}} = 1.53$) and IRAS04286–6937 at 25 μm ($F_{\text{rev}}/F_{\text{lit}} = 1.67$).

IRAS counterparts not listed in IRAS-based catalogues may still be found in the original IRAS data. This is because manual extraction and measuring of the data is a more sophisticated technique than the automatic techniques that created the existing catalogues. In particular, manual flux-density determination enables the background flux levels to be estimated

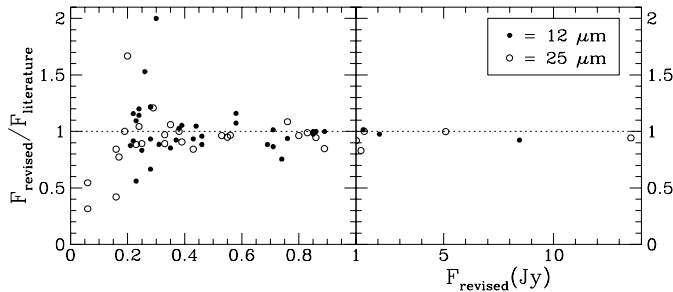


Fig. 1. A comparison of the estimates of IRAS flux densities given here and values from the IRAS Point Source Catalogue and Schwing & Israel (1990), at 12 (solid symbols) and 25 μm (open symbols).

and subtracted better, yielding more reliable photometry. The only sources from our ISO sample that could not be detected in the IRAS data at either 12, 25 or 60 μm are GRV0519–6700, SHV0454030–675031 and SHV0524565–694559.

4. ISO observations

The programme stars were observed with ISO at 12, 25 and 60 μm (chopped measurements) and with PHOT-S as part of a Guaranteed Time programme under proposals NTMCAGB1 and NTMCAGB2, and at 60 μm with mapping mode and CAM-CVF as part of an Open Time programme under proposal LM-CSPLECT.

The 12 μm photometry was mostly obtained using the ISO-CAM instrument (Cesarsky et al. 1996) in staring mode with a 3'' pixel field of view in beam LW-s and using the LW10 filter (\sim IRAS 12 μm). We did 25 exposures of each 2.1 s duration, after a number of read-outs to stabilise the detector (ranging from 10 to 34 frames depending on the expected source flux density). The gain was 2 in most cases, but 1 in the case of sources that were expected to be relatively bright: HV12501 and 996, IRAS04496–6958, 04545–7000, 05003–6712, 05112–6755, 05348–7024 and 05568–6753, and WOH SG374. For most stars this resulted in a clear detection with S/N ratios of 10 to 100. In total 44 sources were observed with ISOCAM at 12 μm .

For sources that were expected to be stronger than 0.5 Jy and which would therefore saturate the ISOCAM detectors with the LW10 filter, the 12 μm photometry was obtained with the ISOPHOT instrument (Lemke et al. 1996) using the 11.5 filter (\sim IRAS 12 μm). These observations were done using triangular chopping with a chopper throw of 90''. The aperture used for the observations was 52'' in diameter. Integration times were 32 s on-source (and the same off-source), except for IRAS05294–7104 that we integrated 64 s. A total of 13 sources were observed in this mode. For 53 sources we obtained PHOT-P photometry at 25 μm using the 25 filter (\sim IRAS 25 μm), triangular chopping with a chopper throw of 90'', and an aperture of 52''. Integration times ranged from 32 to 256 s, depending on the expected flux density. In our Guaranteed Time programme we finally observed 40 objects with ISOPHOT at 60 μm using the PHOT-C100 camera and filter 60 (\sim IRAS 60 μm) and triangular chopping with a 150'' chopper throw. Integration times

ranged from 32 to 128 s, depending on the expected flux density. Unfortunately due to the reduced in-orbit sensitivity of the instrument and the problems with the calibration of the chopped measurements (especially for PHOT-C), we discovered after most observations had already been carried out that this was not the best observing strategy for the 60 μm photometry. Therefore, 7 objects were observed again in the Open Time using PHOT-C100 and filter 60 in raster mapping mode, with 3×3 rasters and 45'' raster steps in X and Y directions (spacecraft coordinates). The integration time per raster point was 128 seconds.

In order to establish the carbon- or oxygen-rich nature of some of the programme stars we also obtained IR spectra for a number of them. In the Guaranteed Time 15 objects were observed using PHOT-S in staring mode, with integration times of 256 or 512 s (1024 s for HV2379) depending on the expected flux densities. The advantage of this instrument is that its spectral coverage is rather large (2 to 12 μm) at a reasonable resolution (\sim 90). The sensitivity of the PHOT-S instrument, however, limits the detectability to sources with 12 μm flux densities above \sim 0.3 Jy. Furthermore, using staring observations the background cannot easily be determined. In this spectral region the diffuse emission is dominated by the zodiacal emission, which, according to IRAS measurements, amounts to about \sim 0.1 Jy in the PHOT-S aperture at 10 μm .

Considering this, we decided to obtain CAM-CVF spectra for 12 objects with a pixel field-of-view of 6'' in beam LW-1. We did 25 exposures of 2.1 s each at gain 2, after 50 read-outs to stabilise the detector. The unprecedented sensitivity of the ISO-CAM instrument allows the observer to obtain spectra even for sources as faint as 100 mJy at 12 μm . Because of the long duration of a CVF observation, the spectral coverage chosen was only 7 to 9.2 μm (with step 4) in LW-CVF1 and 9 to 14.1 μm (with step 2) in LW-CVF2, at a spectral resolution of \sim 40. A big advantage of the CAM-CVF is that the spectra are obtained using an imaging technique. Therefore, a background spectrum was obtained simultaneously. These background spectra can be used to correct the PHOT-S spectra. We also obtained observations of 3 objects for which PHOT-S spectra had already been taken, in order to cross-check the results from the different instruments.

4.1. Near-IR photometry

Near-IR photometry was determined for each star at the time of the ISO observation, by interpolating near-IR lightcurves from our monitoring campaign at the South African Astronomical Observatory (SAAO) at Sutherland, South Africa (Whitelock et al., in preparation). Nearly always the lightcurve was sampled close in time to the ISO observation, but occasionally some extrapolation was necessary. The quoted uncertainties include an estimate, for each star, of the error introduced by the inter/extrapolation. For TRM45 and for the H-band magnitude of IRAS05360–6648 we have made use of the near-IR lightcurves and photometry presented by Wood (1998), after transformation to the SAAO system using Carter (1990). The near-IR photom-

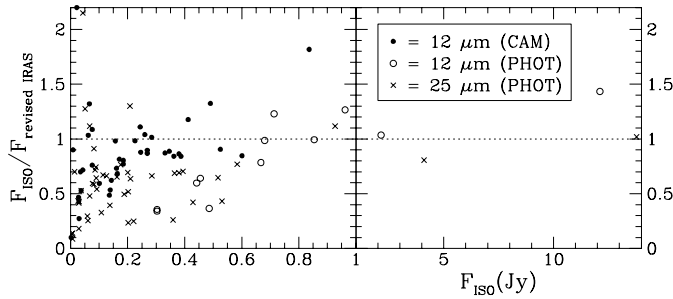


Fig. 2. Comparison between ISO and our revised IRAS flux densities.

entry is listed in Table 4, along with the ISO photometry and the Julian Dates of the ISO spectroscopy.

No near-IR counterparts could be identified with IRAS 05568–6753 and 05289–6617. Two stars with near-IR colours much like those of unobscured M-type stars were monitored in the near-IR, but they show no variability.

5. ISO results and comparison with IRAS photometry

The data were reduced using the PHOT and CAM Interactive Analysis software packages: PIA (Gabriel et al. 1997) version V7.1.2(e) and CIA (Ott et al. 1997) version V3.0, respectively. For a general description of the data and reduction methods see the ISOPHOT Data Users Manual (Laureijs et al. 1998), and the ISOCAM Observer’s Manual (1994) and ISOCAM Data Users Manual (Siebenmorgen et al. 1998). Details of the steps undertaken in reducing so-called Edited Raw Data (ERD) products to the finally derived flux densities and spectra can be found in Appendices A (photometry) and B (spectroscopy). The resulting ISO photometry is listed in Table 4, and the ISO spectra are presented in Figs. 4 & 5.

The flux densities at 12 and 25 μm for the stars that were detected both by IRAS and ISO (Tables 3 & 4) are compared in Fig. 2. A bright regime where ISO and IRAS are consistent can be distinguished from a faint regime where ISO flux densities are systematically lower than IRAS flux densities. CAM is consistent with IRAS down to fainter levels ($\sim 0.2\text{ Jy}$) than PHOT ($\sim 0.6\text{ Jy}$). PHOT seems to under-estimate flux densities at levels between 0.2 and 0.6 Jy by a factor \sim two. Below 0.2 Jy, both CAM and PHOT yield flux densities $\sim 0.6 \times$ IRAS.

Flux density under-estimation may be caused by the difficulty of the detectors to respond to low signals. CAM 12 μm flux densities below $\sim 0.2\text{ Jy}$ may have been under-estimated as the κ - σ method does not adequately correct for non-stabilised signals if stabilisation is not reached well within less than half the integration time. The 12 and 25 μm PHOT measurements, although employing different detector materials, show exactly the same trend. The 12 (either CAM or PHOT) and 25 μm observations were performed in the same orbit. Default responsivities for the 12 and 25 μm PHOT measurements were thought to be (much) lower in 1996 than in the current calibrations. Adopting those early values, the ISOPHOT photometry would be consistent with the IRAS photometry to a high degree. Subsequent revisions of the default responsivities have led to higher values,

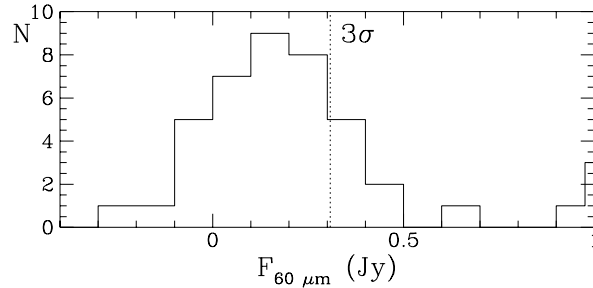


Fig. 3. Histogram of the distribution of ISO 60 μm flux densities (chopped measurements). The dotted vertical line indicates 3- σ flux density derived from the distribution of negative flux densities. All flux densities over 1 Jy are piled up in the last bin.

approaching the values we obtain from the (chopped) FCS measurements. The ratio of ISO and IRAS flux densities at 25 μm is 0.60 ± 0.06 for the 24 sources with ISO measurements before orbit 190, and 0.68 ± 0.09 for the 21 sources measured after orbit 190. These ratios are very similar, despite the large differences in median IRAS flux density between these two samples: 0.41 and 0.14 Jy, respectively.

However, the discrepancy between the ISO and IRAS data may not be as great as it appears if we take plausible selection effects into account. The stars in our sample were largely selected on the basis of their IRAS flux density, but many of them were only just detected by IRAS. It is therefore likely that they were near the maximum of their pulsation cycles at the time of the IRAS observation. In contrast, they will have been at random phases when the ISO observations were made. This will lead to a systematic difference between the IRAS and ISO flux densities for faint sources. A similar effect may explain the discrepancy between the PHOT and CAM behaviour for sources with flux densities in the range 0.2 to 0.6 Jy, as the brighter sources were selected for measurement with PHOT and the fainter sources with CAM. Ground-based 10 μm (N-band) magnitudes of a subset of our ISO targets were on average $\sim 30\%$ fainter than measured by IRAS at 12 μm (Paper IV). Although we explained this in terms of differences between the N-band and IRAS 12 μm filters, it may actually reflect the same discrepancy seen between the ISO and IRAS photometry. Variability cannot be the complete explanation, though: for instance, the sources IRAS04407–7000, 4516–6902 and 05003–6712 were all near the maxima in their K- and L-band lightcurves at the time of the ISO photometry, yet their PHOT 25 μm flux densities of 0.584, 0.380, and 0.210 Jy, respectively, are still fainter than the IRAS flux densities by factors of 0.77, 0.69, and 0.64, respectively. Interestingly, Reid et al. (1990, their Fig. 5) show that for $F_{12,25} \lesssim 0.3\text{ Jy}$ both the PSC and Schwering & Israel (1990) over-estimate flux densities for point sources in the LMC by typically 20 to 50%. They attribute this to source confusion resulting from the large beam width and crowdedness in typical LMC fields.

A histogram of the distribution of ISO 60 μm flux densities (Fig. 3), leaving out the mapping observations, illustrates the detection rate. Considering negative flux densities indicat-

Table 4. ISO 12, 25 and 60 μm photometry (in Jy). The near-IR magnitudes for the ISO-epochs is deduced from light curves obtained at SAAO ($JD - 2, 450, 000 = \text{orbit} + 38$). Values in parentheses are $1-\sigma$ errors. The last column indicates when a PHOT-S or CAM-CVF spectrum was taken.

Star	JD	$J[mag]$	$H[mag]$	$K[mag]$	$L[mag]$	$F_{12}(\text{CAM})$	$F_{12}(\text{PHOT})$	$F_{25}(\text{PHOT})$	$F_{60}(\text{chop})$	$F_{60}(\text{map})$	Spectrum
GRV0519–6700	318	12.63(0.03)	11.36(0.02)	10.67(0.02)		0.004(0.001)					
HV12070	274	10.03(0.02)	8.98(0.02)	8.68(0.02)	8.24(0.03)	0.043(0.004)		–0.023(0.003)			
	787	10.30(0.10)	9.20(0.10)	8.80(0.10)	8.30(0.10)						CAM-CVF
HV12501	754	8.80(0.05)	8.00(0.05)	7.75(0.05)	7.30(0.05)	0.185(0.005)		0.067(0.018)	0.260(0.108)		
HV2360	754	9.00(0.05)	8.15(0.05)	7.75(0.05)	7.20(0.05)	0.331(0.003)		0.138(0.019)	0.207(0.042)		
HV2379	288	12.68(0.03)	12.05(0.04)	11.40(0.04)	9.70(0.10)	0.038(0.002)			–0.027(0.048)		PHOT-S
	626		13.20(0.40)	11.90(0.20)		0.035(0.001)					
	729		13.20(0.40)	11.90(0.20)		0.032(0.001)		0.014(0.005)			CAM-CVF
HV2446	288	10.25(0.02)	9.23(0.02)	8.80(0.02)	8.35(0.04)	0.066(0.001)		0.043(0.005)	0.109(0.056)		
	622	10.60(0.10)	9.60(0.10)	9.10(0.10)	8.35(0.05)					0.361(0.135)	
	754	10.10(0.02)	9.04(0.02)	8.67(0.02)	8.06(0.02)						CAM-CVF
HV5870	754	9.34(0.02)	8.40(0.02)	8.10(0.02)	7.60(0.04)	0.269(0.002)		0.092(0.008)	0.090(0.355)		
HV888	195	8.10(0.01)	7.20(0.01)	6.89(0.01)	6.46(0.02)		0.713(0.037)	0.201(0.012)	–0.237(0.626)		PHOT-S
HV916	209	8.55(0.03)	7.60(0.03)	7.25(0.02)	6.80(0.02)	0.380(0.004)		0.176(0.015)	0.065(0.171)		
HV996	163	8.93(0.01)	8.01(0.01)	7.58(0.01)	6.83(0.01)	0.601(0.006)		0.364(0.026)	0.326(0.074)		PHOT-S
IRAS04286–6937	217		13.00(0.05)	11.25(0.05)	9.10(0.05)	0.136(0.002)		0.059(0.013)	–0.101(0.130)		
IRAS04374–6831	195		13.60(0.05)	11.40(0.04)	8.80(0.03)	0.185(0.003)		0.086(0.027)	0.228(0.136)		PHOT-S
	701		13.60(0.10)	11.40(0.10)	8.90(0.10)					0.309(0.069)	
IRAS04407–7000	217	10.18(0.03)	8.92(0.03)	8.18(0.03)	7.30(0.05)		0.962(0.024)	0.584(0.031)	0.125(0.088)		
	605	11.70(0.05)	10.20(0.05)	9.20(0.05)	8.10(0.05)					0.473(0.132)	
IRAS04496–6958	195	13.00(0.05)	10.90(0.05)	9.50(0.04)	7.70(0.04)	0.269(0.002)		0.126(0.010)	0.252(0.154)		PHOT-S
	605	12.40(0.05)	10.40(0.05)	8.95(0.05)	7.60(0.05)						CAM-CVF
IRAS04498–6842	217	10.95(0.05)	9.65(0.05)	8.70(0.02)	7.70(0.02)		0.486(0.013)	0.221(0.028)	0.292(0.112)		
IRAS04509–6922	217	11.50(0.05)	10.00(0.04)	9.15(0.04)	8.10(0.04)		0.303(0.011)	0.202(0.028)	–0.021(0.231)		
IRAS04516–6902	202	10.50(0.03)	8.96(0.03)	8.24(0.03)	7.25(0.03)		0.854(0.026)	0.380(0.051)	0.349(0.135)		
IRAS04530–6916	202	13.65(0.05)	11.60(0.04)	9.73(0.02)	7.60(0.03)		2.144(0.079)	4.105(0.054)	37.656(2.639)		
IRAS04539–6821	229		14.30(0.05)	11.80(0.04)	8.80(0.10)	0.244(0.002)		0.089(0.013)	0.106(0.053)		
IRAS04545–7000	195		11.75(0.03)	9.40(0.02)	7.15(0.03)	0.836(0.008)		0.927(0.027)	0.641(0.192)		PHOT-S
	605		12.80(0.10)	10.30(0.10)	8.10(0.10)					0.286(0.206)	
IRAS04557–6753	229		14.60(0.05)	12.45(0.04)	9.60(0.05)	0.164(0.002)		0.090(0.027)	–0.072(0.137)		
IRAS05003–6712	229	12.30(0.05)	10.65(0.05)	9.45(0.05)	8.15(0.05)	0.362(0.003)		0.210(0.007)	0.173(0.079)		PHOT-S
IRAS05009–6616	229	14.70(0.10)	12.65(0.05)	10.70(0.05)	8.45(0.05)	0.284(0.003)		0.082(0.017)	–0.032(0.047)		
IRAS05112–6755	288		14.70(0.10)	12.00(0.05)	8.80(0.05)	0.414(0.004)			0.078(0.133)		PHOT-S
	629		14.70(0.10)	11.90(0.05)	8.65(0.05)	0.360(0.003)					PHOT-S
IRAS05113–6739	288		14.35(0.05)	12.12(0.03)	9.06(0.02)	0.316(0.003)			0.398(0.115)		
	629		13.90(0.10)	11.60(0.10)	8.75(0.05)	0.209(0.002)					
	729		13.90(0.05)	11.60(0.05)	8.75(0.05)	0.254(0.002)		0.067(0.013)			
IRAS05128–6455	628	13.60(0.10)	12.10(0.10)	10.55(0.05)	8.55(0.05)	0.226(0.002)		0.061(0.008)			PHOT-S
IRAS05190–6748	288			13.10(0.05)	9.70(0.10)	0.346(0.003)		0.163(0.022)	0.190(0.060)		PHOT-S
IRAS05289–6617	209					0.157(0.002)		0.202(0.009)	0.382(0.049)		
	668									0.281(0.069)	
	729										CAM-CVF

ing non-detection, and assuming a Gaussian distribution around zero flux density for non-detections, we estimate a $1-\sigma$ detection to have 0.103 Jy. There are 12 sources with flux densities exceeding $3-\sigma$, i.e. probable detections. This does not take into account the large errors on some of the individual measurements, and a $3-\sigma$ detection may still turn out to be spurious (an example is WBP14). On the other hand, the distribution below $3-\sigma$ is certainly skewed towards positive flux densities. Projecting the negative flux density distribution onto the positive domain, we estimate that there are probably 17 more detections between 0 and $3-\sigma$, and a total of 14 non-detections.

In the IRAS 60 μm data we found 8 detections and 17 tentative detections (Table 3). The 0.1 Jy assigned to the faintest IRAS 60 μm flux densities compares well with the ISO $1-\sigma$ detection threshold of the chopped measurements. Of the 8 IRAS 60 μm detections 6 have ISO chopped measurements, all of which yield higher flux densities than IRAS — by a factor 1.8 on average. This is in contrast to the 12 and 25 μm photometry, where ISO flux densities are generally lower than those measured by IRAS.

The 14 ISO chopped measurements of IRAS tentative detections also yield higher flux densities than did IRAS — by a factor of 1.5 on average, although some individual ISO measurements are fainter than the IRAS ones. None of these ISO measurements is negative, indicating that many of the IRAS 60 μm tentative detections are indeed real.

The 7 mapping observations all agree with the chopped measurements within $2-\sigma$, although these errors can be large. There is no tendency for one of these two methods to yield higher flux densities than the other. As we do not expect strong variability at 60 μm , which traces cool dust some distance from the stars, flux densities from mapping and chopped measurements are averaged. The error estimates of the mapping measurements are systematically larger than those of the chopped measurements. This may be due to the fact that, for the mapping data, the flux density of the star was determined from the inner 3×3 pixels. The contribution of the background to these 9 pixels is considerable. Also, the reliability of the error estimate for the central pixel in the chopped data as produced by PIA is unknown. There

Table 4. (continued) The near-IR photometry of Wood (1998) is used for TRM45 and in part for IRAS05360–6648 (H-band), after transformation to the SAAO system (Carter 1990).

Star	<i>J</i> <i>D</i>	<i>J</i> [mag]	<i>H</i> [mag]	<i>K</i> [mag]	<i>L</i> [mag]	<i>F</i> ₁₂ (CAM)	<i>F</i> ₁₂ (PHOT)	<i>F</i> ₂₅ (PHOT)	<i>F</i> ₆₀ (chop)	<i>F</i> ₆₀ (map)	Spectrum
IRAS05294–7104	754	11.80(0.05)	10.00(0.05)	8.90(0.05)	7.60(0.05)		0.680(0.045)	0.394(0.035)	0.079(0.097)		
IRAS05295–7121	209		13.85(0.05)	11.75(0.05)	9.35(0.05)	0.143(0.001)		0.007(0.011)	0.233(0.074)		
IRAS05298–6957	209			11.60(0.20)	8.60(0.20)		0.303(0.015)	0.359(0.014)	0.414(0.279)		PHOT-S
	729	14.10(0.20)	12.50(0.10)	11.10(0.10)	8.50(0.20)						CAM-CVF
IRAS05300–6651	209		14.70(0.20)	12.20(0.10)	9.10(0.10)	0.246(0.003)		0.114(0.017)	0.068(0.049)		
IRAS05329–6708	163	17.00(0.20)	12.70(0.10)	10.40(0.05)	8.25(0.05)		0.442(0.018)	0.531(0.035)	0.479(0.082)		PHOT-S
IRAS05348–7024	202		13.60(0.30)	11.60(0.20)	8.70(0.20)	0.525(0.005)		0.208(0.031)	0.170(0.108)		
	732		13.80(0.30)	12.70(0.20)	9.30(0.20)						CAM-CVF
IRAS05360–6648	202		15.00(0.40)	12.30(0.05)	9.50(0.10)	0.171(0.002)		0.082(0.013)	0.174(0.067)		
IRAS05402–6956	217		13.50(0.10)	10.60(0.05)	8.00(0.04)		0.455(0.020)	0.429(0.022)	0.944(0.288)		
	662	14.40(0.10)	11.45(0.05)	9.40(0.03)	7.15(0.03)					–0.245(0.527)	
	782	14.50(0.10)	11.50(0.05)	9.50(0.05)	7.25(0.05)						CAM-CVF
IRAS05506–7053	173		16.00(0.30)	13.30(0.10)	10.00(0.10)				0.109(0.062)		
	228		16.40(0.30)	13.60(0.10)	10.30(0.10)		–0.035(0.017)	0.029(0.015)	0.167(0.073)		
IRAS05558–7000	209	11.90(0.04)	10.10(0.04)	8.90(0.03)	7.60(0.04)		0.667(0.011)	0.517(0.016)	0.291(0.100)		PHOT-S
	781	13.50(0.05)	11.60(0.03)	10.03(0.01)	8.20(0.05)						CAM-CVF
IRAS05568–6753	186					0.412(0.004)		0.285(0.008)	0.383(0.073)		PHOT-S
SHV0454030–675031	318	14.20(0.10)	12.67(0.04)	11.85(0.03)		0.006(0.002)					
SHV0500193–681706	229	14.00(0.20)	12.00(0.10)	10.70(0.10)	9.50(0.10)	0.030(0.005)		0.030(0.016)	0.098(0.026)		
	754	13.10(0.10)	11.45(0.05)	10.25(0.05)	9.00(0.05)						CAM-CVF
SHV0500233–682914	229	13.05(0.05)	11.30(0.05)	10.00(0.05)	8.50(0.05)	0.076(0.001)		0.004(0.033)	–0.004(0.097)		
	729	13.30(0.10)	11.40(0.10)	10.20(0.05)	8.60(0.05)						CAM-CVF
SHV0502469–692418	304	12.93(0.03)	11.61(0.02)	10.81(0.02)	10.30(0.05)	0.002(0.001)					
SHV0521050–690415	788	11.07(0.02)	9.77(0.02)	9.23(0.02)	8.40(0.10)	0.062(0.004)		–0.011(0.014)			
SHV0522023–701242	788	12.60(0.10)	11.60(0.10)	11.40(0.10)		0.001(0.001)		0.003(0.021)			
SHV0522118–702517	217	13.00(0.20)	12.00(0.20)	11.00(0.20)	9.70(0.20)	0.028(0.001)		0.007(0.002)	0.170(0.125)		
SHV0524565–694559	217	12.50(0.04)	11.40(0.05)	10.75(0.05)		0.003(0.001)					
SHV0526001–701142	217	13.50(0.10)	12.00(0.10)	10.45(0.05)	9.15(0.05)			–0.019(0.030)	0.051(0.063)		
SHV0530323–702216	788	11.80(0.10)	10.80(0.10)	10.35(0.05)		0.008(0.002)		0.008(0.009)			
SHV0535442–702433	782	12.90(0.20)	11.50(0.10)	10.65(0.05)	10.30(0.20)	0.009(0.001)		0.029(0.022)			
SP77 30–6	195	10.80(0.10)	9.60(0.10)	9.20(0.10)	8.50(0.10)	0.139(0.001)		0.077(0.018)	0.225(0.073)		
	794	10.30(0.10)	9.30(0.10)	8.80(0.10)	8.20(0.10)						CAM-CVF
TRM45	788	16.20(0.20)	13.60(0.10)	11.55(0.05)	9.50(0.10)	0.076(0.001)		0.037(0.007)			
TRM72	788	15.22(0.20)	12.81(0.03)	10.96(0.02)	8.60(0.05)	0.161(0.001)		0.026(0.025)			
TRM88	788	13.50(0.10)	11.78(0.02)	10.24(0.02)	8.55(0.05)	0.101(0.001)		0.051(0.014)			
WBP14	209	13.35(0.05)	11.60(0.05)	10.55(0.03)	9.50(0.10)	0.022(0.001)		–0.005(0.011)	1.372(0.539)		
	616	13.40(0.10)	11.60(0.10)	10.55(0.05)	9.50(0.05)					0.211(0.293)	
WOH G64	229	9.58(0.02)	7.96(0.02)	6.98(0.02)	5.32(0.02)		12.112(0.965)	13.786(0.354)	4.647(0.298)		PHOT-S
WOH SG374	788	9.90(0.02)	9.10(0.02)	8.64(0.02)	7.69(0.05)	0.490(0.005)		0.188(0.020)			

is great difficulty in extracting reliable photometry and associated errors from either mapping or chopped measurements at 60 μm , for stellar sources in fields like the LMC. This is mainly due to the complex background and limited spatial resolution of PHOT at these wavelengths. IRAS05289–6617 has a very smooth background, being situated in the line-of-sight to the supergiant shell LMC4 (Meaburn 1980). Indeed, ISO mapping and chopped measurements are relatively precise for this source, and agree nicely with the 60 μm flux density measured from the IRAS data.

6. Discussion

6.1. Chemical types from ISO spectroscopy

The presence or absence in the ISO spectra (Figs. 4 & 5) of discrete dust emission and molecular absorption bands can be used to distinguish between carbon- and oxygen-rich circumstellar envelopes (e.g. Merrill & Stein 1976a,b,c). The results are summarised in Table 5.

Amorphous oxygen-rich dust may give rise to strong and broad silicate emission between ~ 8 and 13 μm , peaking at $\sim 9.7 \mu\text{m}$ (the exact location may differ from this by a few tenths of

μm). The late-M stars HV2446, 888, 996, and SP77 30–6 have prominent silicate emission. In optically thick cases the silicate feature turns into absorption. All spectra of OH maser sources show the silicate feature in self-absorption: IRAS04545–7000, 05298–6957, 05329–6708, 05402–6956, and WOH G64.

Oxygen-rich molecules do not provide clear diagnostics of the chemical type of CSEs at our signal-to-noise and spectral resolution. We already mentioned that shallow absorption around 3 μm in oxygen-rich sources is most likely due to an artifact in the responsivities, rather than H₂O ice.

Crystalline carbon-rich dust sometimes gives rise to a SiC (graphite) emission feature peaking at $\sim 11.3 \mu\text{m}$, and narrower than the silicate feature. The CVF spectrum of IRAS05289–6617 (Fig. 4) shows the best example of this.

Carbon-rich molecules have several strong absorption bands in our spectral region, all from HCN and C₂H₂. The strongest is at 3.1 μm , but the problem with the responsivities limits the number of unambiguous detections to one (IRAS04496–6958). Related, but weaker, absorption is visible at 3.8 μm . More absorption bands are located around 5, 8 and 14 μm . Unfortunately, the 5 μm band falls entirely in the blind spectral region

Table 5. Chemical types. Optical spectra (Opt Sp) include objective prism and CCD spectroscopy up to $\sim 1 \mu\text{m}$. ISO spectroscopy (ISO Sp) comprises PHOT-S and CAM-CVF observations. IR colour-colour diagrams (IR col) can in some cases be reasonably conclusive too: we here use $(K - [12])$ and $([12] - [25])$ versus $(K - L)$ diagrams. At radio wavelengths, OH, SiO and/or H₂O maser emission is detected from some oxygen-rich sources.

Star	Opt Sp	ISO Sp	IR col	Maser
GRV0519–6700	C		carbon?	
HV12070	MS3/9	oxygen?	?	
HV12501	M1.5		oxygen	
HV2360	M2 Ia		oxygen	
HV2379	C	SiC?	carbon	
HV2446	M5e	silicate	oxygen	
HV5870	M4.5/5		oxygen	
HV888	M4 Ia	silicate	oxygen	
HV916	M3 Iab		oxygen	
HV996	M4 Iab	silicate	oxygen	
IRAS04286–6937			carbon	
IRAS04374–6831		SiC?	carbon	
IRAS04407–7000			oxygen	yes
IRAS04496–6958	C	car+sil?	carbon	
IRAS04498–6842			oxygen	
IRAS04509–6922	M10		oxygen	
IRAS04516–6902	M9		oxygen	
IRAS04530–6916			oxygen	
IRAS04539–6821			carbon	
IRAS04545–7000		silicate	oxygen	yes
IRAS04557–6753			carbon	
IRAS05003–6712		silicate?	oxygen	
IRAS05009–6616			carbon	
IRAS05112–6755		carbon?	carbon	
IRAS05113–6739			carbon	
IRAS05128–6455		carbon?	carbon	
IRAS05190–6748		carbon?	carbon	
IRAS05289–6617		SiC	?	
IRAS05294–7104			oxygen	
IRAS05295–7121			carbon	
IRAS05298–6957		silicate	oxygen	yes
IRAS05300–6651			carbon	
IRAS05329–6708		silicate	oxygen	yes
IRAS05348–7024		SiC	carbon	
IRAS05360–6648			carbon	
IRAS05402–6956		silicate	oxygen	yes
IRAS05506–7053			oxygen	
IRAS05558–7000		silicate	oxygen	
IRAS05568–6753		carbon?	?	
SHV0454030–675031	C		carbon	
SHV0500193–681706		carbon	carbon	
SHV0500233–682914		SiC?	carbon	
SHV0502469–692418	C		carbon?	
SHV0521050–690415	C		carbon	
SHV0522023–701242	M3		?	
SHV0522118–702517	S?		carbon	
SHV0524565–694559	MS5		?	
SHV0526001–701142	C		carbon	
SHV0530323–702216	M6		oxygen	
SHV0535442–702433	C		?	
SP77 30–6	M8	silicate	oxygen	

Table 5. (continued)

Star	Opt Sp	ISO Sp	IR col	Maser
TRM45			carbon	
TRM72	C		carbon	
TRM88	C		carbon	
WBP14	C		carbon	
WOH G64	M7.5	silicate	oxygen	yes
WOH SG374	M6		oxygen	

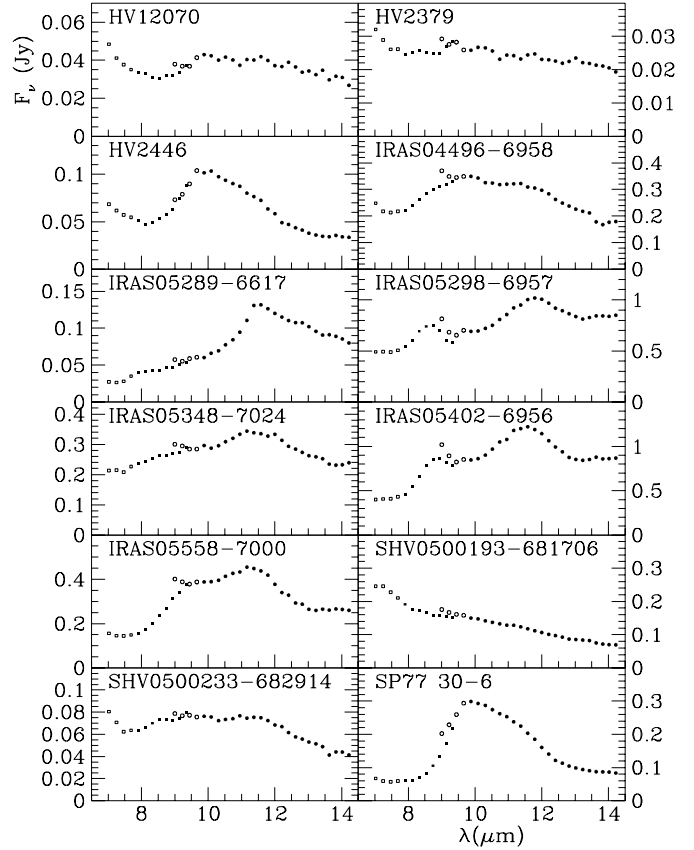


Fig. 4. The CAM-CVF spectra of obscured AGB stars in the LMC. Open symbols represent spectro-photometric points that are prone to have flux densities that are over-estimated due to stabilisation difficulties. The spectral shape is best represented by the solid symbols (squares for the short-, disks for the long-wavelength region). Emission and/or absorption centred at $\sim 9.7 \mu\text{m}$ is indicative of oxygen-rich dust (e.g. IRAS05402–6956 and SP77 30–6), whereas carbon-rich dust may show emission at $\sim 11.3 \mu\text{m}$ (e.g. IRAS05289–6617). A featureless continuum around $10 \mu\text{m}$ also strongly suggests carbon-rich dust (e.g. SHV0500193–681706).

of PHOT-S. The 8 and $14 \mu\text{m}$ bands are at the edges of the CVF spectra and hence difficult to identify.

Some other spectra show merely a featureless dust continuum around $10 \mu\text{m}$. Best examples are the CVF spectrum of SHV0500193–681706 and the PHOT-S spectrum of IRAS05568–6753. These spectra suggest pure amorphous carbon dust emission.

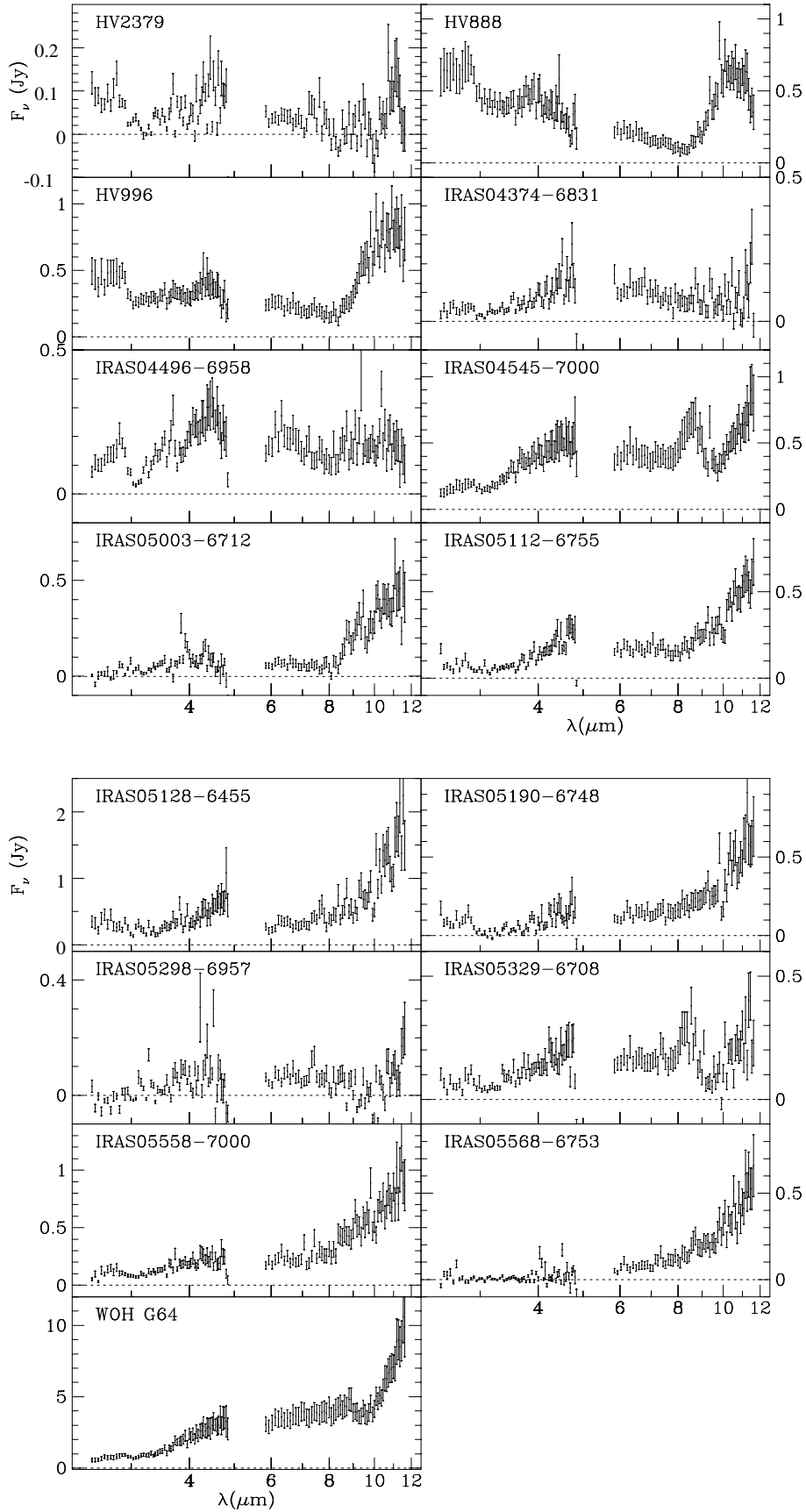


Fig. 5. The PHOT-S spectra of obscured AGB stars (and RSGs) in the LMC. Emission and/or absorption centred at $\sim 9.7 \mu\text{m}$ suggests oxygen-rich dust (e.g. HV888 and IRAS04545–7000). Absorption at $3 \mu\text{m}$ is seen in carbon star photospheres (e.g. IRAS04496–6958), but artifacts in the PHOT-S responsivities also mimic weak depression at $3 \mu\text{m}$ in the spectra of unambiguous oxygen-rich stars (e.g. IRAS04545–7000).

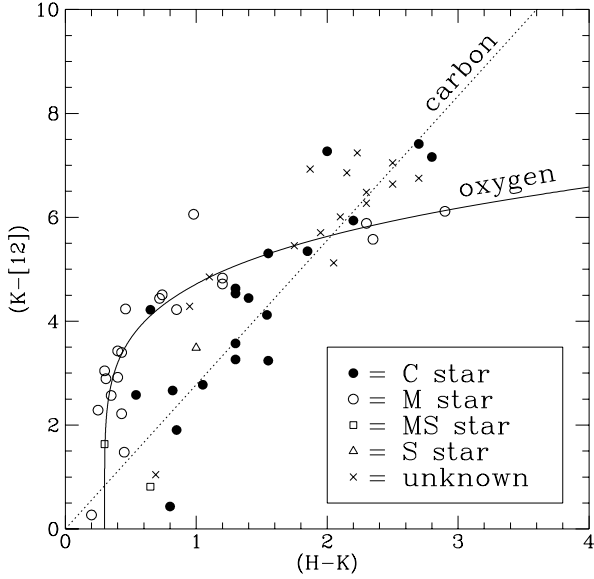


Fig. 6. $(K - [12])$ versus $(H - K)$ diagram. Stars are distinguished by their chemical types inferred from spectroscopic methods: carbon stars (solid disks), M stars (open disks), MS stars (open squares), S stars (open triangles), and stars of which the chemical type is a priori unknown (crosses). Carbon stars and oxygen stars define sequences in this diagram, indicated by a dotted and solid curve, respectively.

6.2. IR colour-colour diagrams

The ISO 12, 25 and $60\ \mu\text{m}$ filters are similar but not identical to the IRAS filters. As the zero-points of these ISO filters are unknown, we adopt here the IRAS zero-points. This results in the following definitions for the (not colour-corrected) mid-IR magnitudes

$$[12] = -2.5 \log(F_{12}/28.3) \quad (1)$$

$$[25] = -2.5 \log(F_{25}/6.73) \quad (2)$$

$$[60] = -2.5 \log(F_{60}/1.19) \quad (3)$$

6.2.1. Diagram of $(K - [12])$ versus $(H - K)$

The $(K - [12])$ versus $(H - K)$ colour-colour diagram separates carbon- from oxygen-rich stars in samples of obscured stars in the MCs (Papers II & IV). Indeed, the distributions of carbon- and oxygen-rich stars using ISO and SAAO photometry define clear sequences in this diagram (Fig. 6). The sequences are fit by eye, with the carbon sequence the same as in Paper IV:

$$(H - K) = 0.36 \times (K - [12]) \quad (4)$$

but the oxygen sequence a simple, yet somewhat steeper function than in Paper IV:

$$(H - K) = 0.3 + 0.0003 \times (K - [12])^5 \quad (5)$$

Although the stars with spectral type M follow the oxygen sequence very well, the carbon stars show a large scatter around the carbon sequence with several carbon stars on or beyond

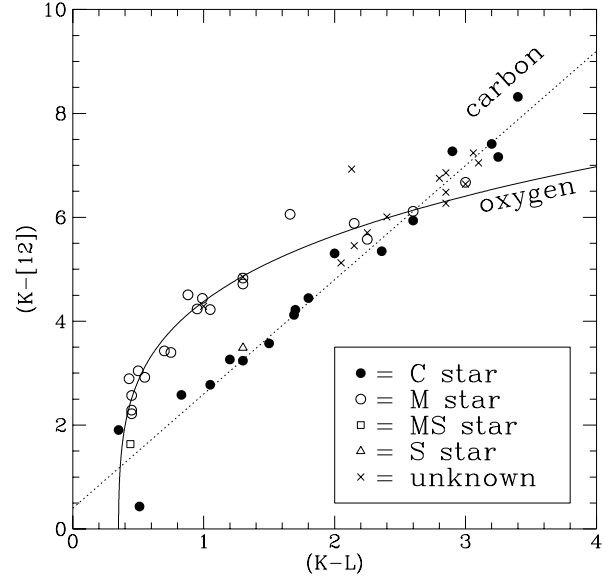


Fig. 7. $(K - [12])$ versus $(K - L)$ diagram. Symbols as in Fig. 6.

the region populated by M stars, at small $(H - K)$ but large $(K - [12])$ magnitudes. This scatter contrasts with the tight carbon sequence that is observed in the Milky Way (Fig. 3 in Paper IV). We suspect that this is in part caused by the severe crowding in some LMC fields, affecting the near-IR aperture photometry. Differences in the strength of absorption in the H-band by carbonaceous molecules may cause additional scatter among carbon stars (Bessell & Wood 1983; Catchpole & Whitelock 1985).

6.2.2. Diagram of $(K - [12])$ versus $(K - L)$

The $(K - [12])$ versus $(K - L)$ colour-colour diagram shows much less scatter around well-defined carbon and oxygen sequences (Fig. 7). This makes it a much more powerful diagnostic diagram than the $(K - [12])$ versus $(H - K)$ diagram in typifying the chemical composition of the circumstellar dust. Noguchi et al. (1991a) introduced a very similar diagnostic using $(L - [12])$ and $(K - L)$ colours. We note, however, that some of the peculiar stars in our $(K - [12])$ versus $(H - K)$ diagram were too blue and hence too faint to be detected in the L-band. Still, the tight sequences prove that both the SAAO and ISO photometry are of good quality when comparing individual stars. We fit (by eye) a linear carbon sequence:

$$(K - L) = \frac{5}{11} \times (K - [12]) - \frac{2}{11} \quad (6)$$

and a superposition of even polynomials for the oxygen sequence:

$$(K - L) = 0.35 + 0.007 \times (K - [12])^2 + 0.0014 \times (K - [12])^4 \quad (7)$$

6.2.3. Diagram of $([12] - [25])$ versus $(K - L)$

Another colour-colour diagram that separates carbon- from oxygen-rich sources is the $([12] - [25])$ versus $(K - L)$ diagram

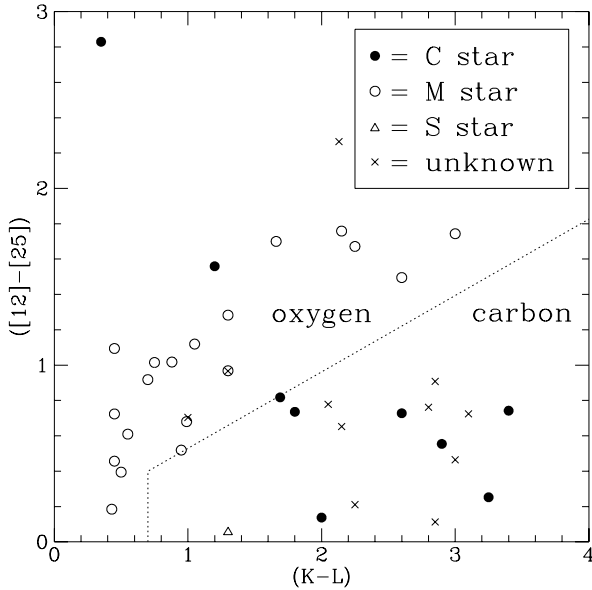


Fig. 8. $([12] - [25])$ versus $(K - L)$ diagram. Symbols are as in Fig. 6. Oxygen-rich sources and carbon stars occupy distinct areas in this diagram. The dividing line (dotted) between stars with carbon- and oxygen-rich dust is taken from Epchtein et al. 1987.

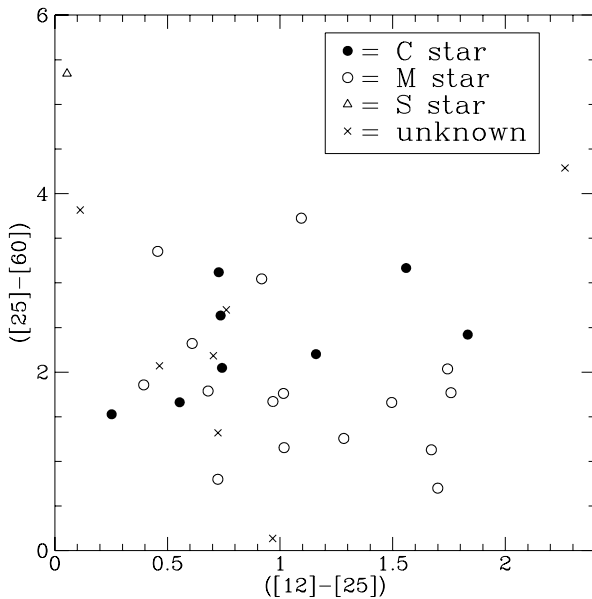


Fig. 9. $([25] - [60])$ versus $([12] - [25])$ diagram. Symbols are as in Fig. 6. Carbon stars are not well separated from oxygen-rich sources, although carbon stars seem to be relatively bright at $60 \mu\text{m}$.

(Fig. 8). The confirmed oxygen-rich sources show a linear relationship between the $([12] - [25])$ and $(K - L)$ colours, possibly flattening out at $(K - L) > 1.5$ mag. The LMC stars generally follow the separation determined for galactic stars (dotted line in Fig. 8, taken from Epchtein et al. 1987).

6.2.4. Diagram of $([25] - [60])$ versus $([12] - [25])$

The aim of obtaining $60 \mu\text{m}$ flux densities for stars in the LMC is mainly to probe the coolest circumstellar dust. The $60 \mu\text{m}$ flux density is expected to increase as prolonged mass loss first extends the CSE and again as reduced mass loss results in a detached shell. This evolution might be seen in $([25] - [60])$ versus $([12] - [25])$ diagrams (Fig. 9, see also van der Veen & Habing 1988). Unfortunately, the accuracy of the ISO photometry at $60 \mu\text{m}$ is not very high for most of these LMC sources, and the diagram contains a lot of scatter.

Perhaps the most obvious thing to learn from this diagram is that carbon stars tend to be relatively bright at $60 \mu\text{m}$, yielding $([25] - [60]) \sim 1.5$ to 3 mag. Although oxygen-rich sources can have similar colours, there are many oxygen-rich sources with $([25] - [60]) < 2$ and $([12] - [25]) > 0.6$ mag, colours not seen for any carbon star in our sample. This is similar to the findings of van der Veen & Habing (1988), but our LMC sources have bluer $([12] - [25])$ and redder $([25] - [60])$ colours than do their Milky Way sources. However, the LMC $([12] - [25])$ colours do not differ much from those discussed by Le Bertre et al. (1994).

6.3. Comments on particular objects

6.3.1. GRV0519–6700

The referee Dr. Peter Wood conveys that an optical spectrum of GRV0519–6700 shows it to be a carbon star, in good agreement with its IR colours of $(H - K) = 0.7$ and $(K - [12]) = 1.0$ mag.

6.3.2. HV12070

The CVF spectrum of HV12070 shows only a hint of the silicate feature, whilst the IR colours cannot distinguish between oxygen- and carbon-rich dust of the optically thin CSE of this MS-type star.

6.3.3. HV2379

The PHOT-S spectrum of HV2379 suggests SiC emission, but its CVF spectrum does not. This may be a result of changes in the properties of the CSE or the dust. Its IR colours leave no doubt about the carbon-rich nature of the dust.

6.3.4. HV2446, 888, 996, and SP77 30–6

These late-M stars all have prominent silicate emission and IR colours that unambiguously indicate oxygen-rich dust.

6.3.5. IRAS04286–6937, 04539–6821, 04557–6753, 05009–6616, 05113–6739, 05295–7121, 05300–6651, 05360–6648, and TRM45 and 72

The position of these objects in the $(K - [12])$ versus $(H - K)$ or $(K - L)$ colour-colour diagrams does not clarify the chemical composition of their CSEs. The $([12] - [25])$ versus $(K - L)$

diagram, however, unambiguously indicates that the dust around these stars is carbon rich. The IR colours of IRAS05113–6739 at the three ISO epochs for this star all lie along the carbon sequences in the $(K - [12])$ versus $(H - K)$ and $(K - L)$ diagrams. Ground-based L-band spectra of IRAS05009–6616 and 05300–6651 show the $3.1 \mu\text{m}$ absorption feature due to HCN and C_2H_2 molecules, indicating carbon-rich photospheres (van Loon et al. 1999).

6.3.6. IRAS04374–6831

The position of IRAS04374–6831 in the $([12] - [25])$ versus $(K - L)$ diagram indicates carbon-rich dust. Its PHOT-S spectrum, which does not clearly reveal the chemical composition of the dust by itself, is then marginally consistent with SiC emission.

6.3.7. IRAS04496–6958

IRAS04496–6958 shows strong absorption by carbonaceous molecules at $3.1 \mu\text{m}$, already known from ground-based L-band spectroscopy (van Loon et al. 1999). Related, but weaker, absorption is visible at $3.8 \mu\text{m}$, and possibly around $8 \mu\text{m}$. Surprisingly, this carbon star has silicate emission too, indicating the presence of oxygen-rich dust (see Trams et al. 1999). Its IR colours indicate carbon-rich dust, hence the oxygen-rich dust is only a minor component.

6.3.8. IRAS04530–6916

With $(K - L) = 2.13$, $(K - [12]) = 6.9$ and $([12] - [25]) = 2.3$ mag, the IR colours of IRAS04530–6916 imply that the dust around this very luminous and red object must be oxygen rich.

6.3.9. IRAS04545–7000, 05298–6957, 05329–6708, 05402–6956, and WOH G64

These OH maser sources all show the silicate feature in self-absorption, and also their IR colours clearly indicate oxygen-rich dust.

6.3.10. IRAS05003–6712

The IR colours of IRAS05003–6712 unambiguously classify the dust as oxygen rich. The PHOT-S spectrum shows a hint of the silicate feature. A ground-based L-band spectrum of this star shows a featureless continuum around $3.1 \mu\text{m}$, indicating an oxygen-rich photosphere (van Loon et al. 1999).

6.3.11. IRAS05112–6755

The dust around IRAS05112–6755 is classified as carbon rich on the basis of the position in the $([12] - [25])$ versus $(K - L)$ diagram. There is a hint of $8 \mu\text{m}$ absorption in the PHOT-S spectrum of IRAS05112–6755. A ground-based L-band spectrum

of this object shows the strong absorption at $3.1 \mu\text{m}$ found in carbon-rich stellar photospheres (van Loon et al. 1999).

6.3.12. IRAS05128–6455 and 05190–6748

The absence of clear indications for the presence of the silicate feature in the PHOT-S spectra of these stars suggest that their dust may be carbon rich, which is also indicated by their $([12] - [25])$ and $(K - L)$ colours.

6.3.13. IRAS05289–6617

The CVF spectrum of IRAS05289–6617 shows prominent SiC emission. Hence it is probably a mass-losing carbon-rich AGB star in the LMC rather than a foreground object. We have not yet identified its near-IR counterpart.

6.3.14. IRAS05348–7024

The CVF spectrum of IRAS05348–7024 shows weak SiC emission. The carbon-rich nature of the dust around this object is also indicated by its position in the $([12] - [25])$ versus $(K - L)$ diagram.

6.3.15. IRAS05506–7053

IRAS05506–7053 is the only star in our sample that could not be detected at $12 \mu\text{m}$. Assuming a $12 \mu\text{m}$ flux density $< 0.03 \text{ Jy}$, the $(K - [12])$ colour would be < 6.2 mag and probably $([12] - [25]) > 1.5$ mag. At $(K - L) = 3.3$ mag, this suggests an oxygen-rich CSE.

6.3.16. IRAS05558–7000

The CVF spectrum of IRAS05558–7000 is similar to the CVF spectra of IRAS05298–6957 and 05402–6956, showing silicate emission that is becoming optically thick at $10 \mu\text{m}$. The IR colours of IRAS05558–7000 unambiguously imply that the dust is oxygen-rich.

6.3.17. IRAS05568–6753

The PHOT-S spectrum of IRAS05568–6753 shows a featureless dust continuum around $10 \mu\text{m}$, suggesting pure amorphous carbon dust emission. The near-IR counterpart of this object has yet to be identified.

6.3.18. SHV0500193–681706

The CVF spectrum of SHV0500193–681706 shows a featureless dust continuum around $10 \mu\text{m}$, suggesting pure amorphous carbon dust emission. The carbon-rich nature of the dust is confirmed by the position in the $(K - [12])$ versus $(K - L)$ diagram. Inaccuracy of its $25 \mu\text{m}$ flux density causes the rather odd position among the oxygen-rich stars in the $([12] - [25])$ versus $(K - L)$ diagram.

6.3.19. SHV0500233–682914

The CVF spectrum of SHV0500233–682914 shows a hint of SiC emission, and also its IR colours clearly indicate that the dust around this star is carbon rich.

6.3.20. SHV0502469–692418, 0522023–701242
and 0524565–694559

The carbon star SHV0502469–692418, the M-type star SHV 0522023–701242 and the MS-type star SHV0524565–694559 are surrounded by an optically thin CSE and hence it is difficult to classify the chemical type of their dust from IR colour-colour diagrams.

6.3.21. SHV0522118–702517

SHV0522118–702517 was tentatively classified an S-type star by Hughes & Wood (1990). Its IR colours are clearly similar to those of carbon stars. This suggests that carbon-rich dust dominates the absorption and emission characteristics of the CSE despite the under-abundance of carbon atoms in its photosphere. Noguchi et al. (1991b) show that the IR colours of the CSE indicate oxygen-rich dust in case of an MS-type star. Also, CS stars show $3\ \mu\text{m}$ absorption from HCN and C_2H_2 molecules, whereas SC stars do not (Catchpole & Whitelock 1985; Noguchi & Akiba 1986). This suggests that carbon chemistry is dominant in CS stars, but not in SC stars. Thus, we identify SHV0522118–702517 with a CS star. Dust-enshrouded S stars — including MS and CS stars — that have $(K - L) > 1$ mag are very rare in the Milky Way, and none are known with $(K - L) > 2$ mag (Noguchi et al. 1991b). Hence, with $(K - L) = 1.3$ mag, SHV0522118–702517 is among the most obscured S stars known.

6.3.22. SHV0530323–702216

The late-M type star SHV0535442–702433 has $([12] - [25]) = 1.56$ mag. Its near-IR colours are rather blue and $(K - L)$ is not expected to be larger than unity. Hence the position of this object in the $([12] - [25])$ versus $(K - L)$ diagram suggests that the dust is oxygen rich.

6.3.23. SHV0535442–702433

The carbon star SHV0535442–702433 is surrounded by an optically thin CSE, and hence the IR colours are difficult to use for classifying the chemical type of the dust. The location among oxygen-rich stars in the $([12] - [25])$ versus $(K - L)$ diagram is caused entirely by the inaccuracy of its $25\ \mu\text{m}$ flux density yielding a spuriously red $([12] - [25]) \sim 3$ mag.

7. Conclusions

ISO spectroscopy is used to determine the chemical type of the dust around obscured cool evolved stars in the LMC. ISO photometry at 12, 25 and $60\ \mu\text{m}$ is presented, together with quasi-

simultaneous near-IR photometry from the ground (SAAO). The accuracy and sensitivity of the ISOPHOT photometry is not much better than can be achieved from properly treated IRAS data. The ISOCAM photometry is much more reliable because it is based on imaging, and an order of magnitude more sensitive than was IRAS. Colour-colour diagrams prove that relative photometry is reliable. A combination of $(K - [12])$ and $([12] - [25])$ versus $(K - L)$ diagrams provide a reliable way of distinguishing between carbon- and oxygen-rich dust, provided the CSE has sufficient optical depth. The combination of ISO spectra and photometry enabled us to securely classify the chemical type of the dust around nearly all stars in our sample. This was previously known for only a minority of the stars. Surprisingly, the $(K - [12])$ versus $(H - K)$ diagnostic diagram contains a lot of scatter especially among carbon stars.

Many of the obscured AGB stars in our sample are carbon stars: 46% amongst the LMC stars that were detected by IRAS (Table 1). M stars were always found to be surrounded by oxygen-rich dust. In particular, all detected OH maser sources show self-absorbed silicate emission. As in the Milky Way, the fact that no M star with carbon-rich dust has ever been found suggests that HBB cannot efficiently turn carbon stars back into oxygen-rich stars. The dust around the dust-enshrouded S star SHV0522118–702517 has the characteristics of carbon-rich material, suggesting it is actually a CS star. Surprisingly, the dust around the carbon star IRAS04496–6958 has a (minor) oxygen-rich component (Trams et al. 1999).

Acknowledgements. We would like to thank everyone at VilSpa (Madrid) for the discussions and advices during the various stages of ISO data reduction, in particular Drs. José Acosta-Pulido, Carlos Gabriel, Rene Laureijs, Thomas Müller, and Bernhard Schulz, and Dr. Péter Ábrahám in Heidelberg. The ISOCAM data presented in this paper was analysed using “CIA”, a joint development by the ESA Astrophysics Division and the ISOCAM Consortium. The ISOCAM Consortium is led by the ISOCAM PI, C. Cesarsky, Direction des Sciences de la Matière, C.E.A., France. The ISOPHOT data presented in this paper was reduced using PIA, which is a joint development by the ESA Astrophysics Division and the ISOPHOT Consortium. We also thank Dr. Romke Bontekoe for help with studying the IRAS data, and the referee Dr. Peter Wood for his suggestions that improved the presentation considerably. We made use of the SIMBAD database, operated at CDS, Strasbourg, France. This research was partly supported by NWO under Pionier Grant 600-78-333.

(JvL: O trabalho mais importante foi feito por um anjo).

Appendix A: ISO photometry

A.1. CAM 12 μm imaging-photometry

The ISOCAM images were corrected for the dark image valid for the corresponding revolution and orbital position of the spacecraft, and corrected for glitches using the multiresolution median transform method. Although the current dark subtraction algorithm produces satisfactory results, we nonetheless also applied our own IDL routine that optimises the dark subtraction by appropriately scaling the dark and flatfield images in a rectangular annulus leaving a 12×12 pixel area centred at the

stellar position on the array. The dark subtraction was improved slightly in some cases, whereas for the majority of the observations there was no significant difference. For each pixel, we applied a κ - σ rejection criterion to the evolution of the signal in time: values that deviate more than 2σ from the time-average were rejected. The images were divided by the default calibration flatfield image to correct for the array pattern in the pixel responsivities, and time-averaged.

Point source photometry was performed on the final image, using our own procedures written within the Munich Interactive Data Analysis Software (MIDAS). We measured the flux density within a circular area (software aperture) around the stellar position, and subtracted the background flux density level determined from a concentric circular annulus between 12 and 14 pixels radius from the stellar position — excluding the pixels near the edge of the 32×32 pixels array where vignetting is evident. We repeated this for different software aperture radii, to create a magnitude profile (MP) of the stellar flux density versus radius. We used the 23 brightest stars — with flux densities ranging from 0.06 to 0.8 Jy — to create a template MP. Comparison of the individual MPs of the stars with the template yielded differential MPs. Where the differential MP is constant with radius, reliable differential magnitudes can be determined. We adopt the standard deviation in these points as $1\text{-}\sigma$ errors on the differential photometry. The strength of the MP-method is the estimation of photometric errors, as well as the selection of the part of the MP that best resembles the PSF. Calibration of the template MP was done using the calibration conversion $4.13 \text{ ADU s}^{-1} \text{ mJy}^{-1}$ (OLP V7 calibration). The template MP was consistent with a synthetic MP created from the known PSF, and indicated an uncertainty of $\sim 1 \text{ mJy}$.

All target stars were detected unambiguously, except for SHV0522023–70124 which was marginally detected. Most were well centred — within about $10''$ — but IRAS05113–6739 (last epoch only), IRAS05295–7121 and TRM45 were off by 20 to $30''$. Seven stars were accompanied by generally weaker additional point sources within the image: HV12501, SHV0500193–681706, 0500233–682914, 0502469–692418, and 0535442–702433, and TRM72 and 88. All of these stars are either HV, SHV, or TRM sources, and the nature of the additional point sources remains a mystery.

A.2. PHOT-P 12 and 25 μm chopped measurements

The measurements each consist of 4 Destructive Readouts (DRs), with 127 Non-Destructive Readouts (NDRs) per ramp. All DRs and the first 8 NDRs per ramp were discarded, because these read-outs are considered unreliable due to the strong impact of the detector reset. The signal corresponding to the source intensity is derived from the slope of the integration ramp. The ramps were linearised to correct for non-linearities in the CRE (Cold-Read-Out Electronics) output voltages and debiasing effects, which mainly affect the long wavelength detectors. We attempted to remove glitches resulting from the impact of high energy particles by applying the two-threshold median filtering technique, using distributions of 32 data points, three iterations,

and thresholds of three standard deviations for flagging and re-accepting. The ramps were subdivided into four sections, so as to be more selective in discarding erroneous read-outs. The first 50% of the signals per chopper plateau were discarded to enable the detector response to stabilise at the level of the source flux density. The chopper plateaus were then treated separately in deglitching the signals. This was done by running a bin with a width of 8 signals over the chopper plateau, taking individual steps, and iterating twice: after maximum/minimum clipping, signals were discarded if they were off by more than three standard deviations. A correction was applied to account for the signal dependence on the reset interval which was used for the read-out sampling. The expected dark current for the orbital position of the spacecraft was subtracted from the data. The differences between on-source and interpolated background signals were corrected for signal losses due to the rapid chopping.

The main source of concern is that the detector response is not constant over time, and depends on the history of the detector illumination and on the levels of source and background. Therefore, careful modeling of the detector behaviour is needed to determine the true source-background signal. At present the quality of our data and the degree of understanding of the detector characteristics is insufficient to allow for such an advanced data reduction. We opted instead for a simpler approach, that also conforms better with the way the standard star observations and flux-density-calibrations were done.

The in-band power was calibrated using the responsivity as derived from an FCS1 internal calibrator measurement reduced in the same way as the scientific measurement, except that background subtraction and chopper frequency correction are not applicable. The ratio of the responsivities determined from FCS1 and default varies between 0.8 and 2.8, averaging 1.4 around orbit 200 and 2.2 around orbit 700. We therefore feel that the FCS1 values reveal the complex detector-history dependence of the responsivity, and hence should be applied to calibrate the in-band power, instead of using the recommended default responsivity for chopped observations.

Finally the median flux density was extracted, correcting for the point source flux density outside of the aperture. The $1\text{-}\sigma$ errors are estimated by quadratic summation of the flux density uncertainty and the error in the responsivity value. The 25 μm flux densities of IRAS05113–6739, IRAS05295–7121 and TRM45 have almost certainly been under-estimated due to off-centering of the source with respect to the ISOPHOT aperture (see the previous subsection about the CAM imaging).

A.3. PHOT-C 60 μm chopped measurements

Observations at a wavelength of 60 μm are severely hampered by the complex and bright sky background compared to the flux density of a typical point source in our sample. The sky in the direction of the LMC varies on a spatial scale of a few arcminutes, due to the presence of molecular cloud complexes within the LMC which are much brighter than circumstellar envelopes at 60 μm . This scale is not much larger than the PSF for a telescope under 1 m diameter.

The measurements each consist of 4 DRs (8 for WOH G64), with the number of NDRs per ramp depending on the expected flux density. Usually we chose 15, 31 or 63 NDRs per ramp, but for IRAS04530–6916 and 05329–6708 and for WOH G64 only 7 and 3, respectively, were chosen. All DRs were discarded, as well as the first 3 or 6 NDRs per ramp in case of 31 or 63 NDRs per ramp, respectively (otherwise only one NDR per ramp was discarded). The ramps were linearised. If a sufficient number of data points were available, glitches were removed by applying the two-threshold median filtering technique, using distributions of 16 data points, three iterations, and thresholds of three standard deviations for flagging and re-accepting. The ramps were subdivided into four sections, provided there were at least four data points per subramp. The first 50% of the signals per chopper plateau were discarded. The signals were deglitched by running a bin with a width of 16 signals over the chopper plateau, taking individual steps, and iterating twice: after maximum/minimum clipping, signals were discarded if they were off by more than three standard deviations. A reset-interval correction was applied. The expected dark current for the orbital position of the spacecraft was subtracted from the data. A correction for vignetting of the 3×3 pixels C100 array was applied. The differences between on-source and interpolated background signals were corrected for signal losses due to the rapid chopping. This correction is very large — a factor of 2.75 — and rather uncertain (35%).

The in-band power was calibrated using the responsivity as derived from an FCS1 internal calibrator measurement done immediately after the scientific measurement. The FCS responsivities were found to resemble the pixel response pattern in the scientific measurement better than the default responsivities did. The FCS measurement was reduced in the same way as the scientific measurement, except that vignetting correction, background subtraction and hence a chopper frequency correction are not applicable. The ratio of the FCS1 and default responsivities varied between 0.8 and 2.0, around a median of 1.3 and with a standard deviation of 0.3. It varied from orbit to orbit and within an orbit, but with no clear time dependence — except that it was larger after orbit 190 than before. This behaviour closely resembles that seen for the PHOT-P detectors.

Finally the median flux densities of the pixels were extracted. The median value of the eight pixels surrounding the central one was subtracted from the central pixel value. Knowing that the central pixel contains 66.35% of the total flux density of a well-centred point source, and the entire C100 array contains 91.75%, a correction factor of 1.5835 was applied. The (internal) $1\text{-}\sigma$ errors are estimated by quadratic summation of the error in the value for the central pixel and $1/\sqrt{8}$ times the median of the differences between background pixels and their median. This does not take into account the uncertainty in the absolute flux-density calibration. The flux density of IRAS05295–7121 has almost certainly been under-estimated due to off-centering of the source with respect to the ISOPHOT aperture (see the earlier subsection about the CAM imaging).

A.4. PHOT-C $60\ \mu\text{m}$ mapping observations

The measurements each consist of 64 DRs, with 63 NDRs per ramp (128 DRs and 31 NDRs per ramp for IRAS05402–6956 and WBP14). All DRs were discarded, as well as the first 3 or 6 NDRs per ramp in case of 31 or 63 NDRs per ramp, respectively. The ramps were linearised. Glitches were removed by applying the two-threshold median filtering technique, using distributions of 32 data points, three iterations, and thresholds of three standard deviations for flagging and re-accepting. The ramps were subdivided into four sections. The first 4 read-outs per raster point were discarded. The signals were deglitched by running a bin with a width of 64 signals through the raster point, taking individual steps, and iterating twice: after maximum/minimum clipping, signals were discarded when they were off by more than three standard deviations. We applied the stability recognition method to derive the signal most likely to be near the true, stabilised one: a bin with a width of 64 signals was run over the measurement, with intervals of 32 signals, and only data within a confidence level of 0.95 were kept. A reset-interval correction was applied. The expected dark current for the orbital position of the spacecraft was subtracted from the data. The 3×3 pixels array was corrected for vignetting.

The in-band power was calibrated by interpolating the responsivities derived from FCS1 internal calibrator measurements made before and after the scientific measurement. Use of the two FCS measurements was found to correct (in part) for drift behaviour of the signal, which was not the case if default responses were used. The FCS measurements were reduced in the same way as the scientific measurement, except that a vignetting correction is not applicable and 16 data points were used for signal deglitching and stability recognition. Finally the median flux densities of the pixels were extracted.

The values of the eight pixels surrounding the central one were replaced by their median value and added to the central pixel value. The values of the sixteen pixels along the rim of the map were also replaced by their median value, and this was taken to be the sky background to be used for correcting the total flux density in the inner 3×3 part of the map. Knowing that the central pixel contains 66.35% of the total flux density of a well-centred point source, and the entire C100 array contains 91.75%, the outer sixteen pixels contain a fraction of the flux density that is somewhere between 0 and 8.25%. Assuming this fraction to be 4.125%, a factor of 1.1182 is derived to correct the background subtracted flux density for the stellar flux density contained in the outer sixteen pixels. The (internal) $1\text{-}\sigma$ errors are estimated by quadratic summation of the error in the value for the central pixel, $8/\sqrt{8}$ times the median of the differences between the eight surrounding pixels and their median, and $9/\sqrt{16}$ times the median of the differences between the outer sixteen pixels and their median. The error in the value for the central pixel was determined by the median of the differences between the values for the pixels that were centred on the star over the course of the mapping, and their median. The error estimate does not take into account the uncertainty in the absolute flux-density calibration.

Appendix B: ISO spectroscopy

B.1. CAM-CVF spectro-photometry

The CAM-CVF cube (X, Y, λ) was corrected for the dark image using a model for the dependence on the revolution and orbital position of the spacecraft, and corrected for glitches by applying a multiresolution median transform. For each pixel, we applied a κ - σ rejection criterion to the evolution of the signal in time: values that deviate more than 2σ from the time-average were rejected. Attempts to correct for the transient behaviour of the signal by applying various models yielded results no better than this method. The images were divided by the default calibration flatfield image to correct for the array pattern in the pixel responsivities, and time-averaged.

The spectra were constructed by obtaining photometry from the images that each correspond to a different position of the CVF. For each target we integrated the signal over the pixels that were significantly above the background level. The number of pixels was limited to avoid sampling excessive background, and ranged from 1, for the faintest, to 9, for the brightest sources. The short- and long-wavelength parts of the CVF were treated separately because the star was often centred at a slightly different position on the array. The background level was determined by taking the median value within a three-pixel wide circular annulus around the star, with an inner radius of three pixels. The stellar flux density was corrected for the wavelength dependence of the PSF. This correction was derived by doing photometry on the PSF with equivalent integration areas but inversely proportional to the wavelength. The first few (~ 4) spectro-photometric points are prone to have flux densities that are over-estimated due to stabilisation difficulties when the CVF scanned from the shortest towards longer wavelengths.

B.2. PHOT-S spectro-photometry

The measurements each consist of 4 or 8 DRs, with 127 NDRs per ramp, except for WOH G64 (16 DRs and 63 NDRs per ramp). All DRs were discarded, as well as the first 12 NDRs per ramp (6 in case of WOH G64). Glitches were removed by applying the two-threshold median filtering technique, using distributions of 32 data points, three iterations, and thresholds of three standard deviations for flagging and re-accepting. The ramps were subdivided into four sections. The first four signals per measurement were discarded. The signals were deglitched by running a bin with a width of 16 signals over the chopper plateau, taking individual steps, and iterating twice: after maximum/minimum clipping, signals were discarded when they were off by more than three standard deviations. The stability recognition method was applied, using an 8-signals wide bin and intervals of 4 signals, keeping only data within a confidence level of 0.95. The time evolution of the signal for each pixel was checked by eye, and obviously bad data that had passed the earlier rejection criteria were removed by hand at this stage. The expected dark current for the orbital position of the spacecraft was subtracted from the data.

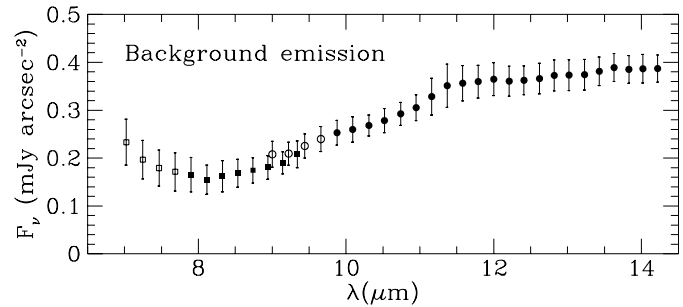


Fig. B1. The CAM-CVF background emission spectrum. Open symbols represent spectro-photometric points that are prone to have flux densities that are over-estimated due to stabilisation difficulties. The spectral shape is best represented by the solid symbols (squares for the short-, disks for the long-wavelength region). The background emission actually arises from the zodiacal dust belt in our Solar system.

The in-band power was calibrated using the default responsivities expected for the orbital position, and finally the mean flux density was extracted, taking into account the amount of flux density lost outside of the aperture. Note that the wavelength dependence of the responsivity shows a bump around $3\mu\text{m}$. When applied to the spectrum of a star, this could introduce an artificial spectral feature which might be interpreted erroneously as absorption due, for instance, to H_2O ice.

The PHOT-S observations did not include a separate measurement of the background. We used the average of the background spectra measured in the CAM-CVF images (Fig. B1, error bars indicate the standard deviation in the set of 12 spectra). This spectrum was used for wavelengths $> 8\mu\text{m}$, and interpolated linearly below $8\mu\text{m}$ to a value of zero at $5\mu\text{m}$ (at shorter wavelengths the background is assumed to be negligible). We ignore the first 4 steps of the CVF filter wheel, that are usually not stabilised. The background is predominantly emission from the zodiacal dust belt in our Solar System. Because of the annual modulation of the zodiacal light level in a particular direction of the sky, the weekly all-sky maps produced by the DIRBE instrument onboard the COsmic Background Explorer (COBE) (<http://www.gsfc.nasa.gov/astro/cobe/#dirbe>) were used to scale the background spectrum to the epochs of the PHOT-S spectra (see Ábrahám et al. 1997). The COBE/DIRBE $12\mu\text{m}$ surface brightnesses for our CVF and PHOT-S observations have standard deviations of 5.5 and 5.9%, respectively. The CVF background spectra yield a standard deviation at $12\mu\text{m}$ of 9.1%. Although the CVF and COBE/DIRBE do correlate, the spread in the CVF background exceeds the variation in the zodiacal light, suggesting that variations in the background emission from the LMC is discernible in our data. The scaled background spectrum is subtracted from the PHOT-S spectra, that were obtained through a $24'' \times 24''$ aperture.

IRAS05112–6755 was observed twice. The spectra look identical, except that the second is a factor 1.5 brighter than the first, independent of wavelength, whilst the near-IR flux densities only differed by $\sim 10\%$. Pointing thresholds were $10''$ and $2''$, respectively, and the star may have been close to the edge of the aperture during the first observation. Flux density levels

in the PHOT-S spectrum of IRAS05298–6957 may have been under-estimated due to off-centering of the star in the PHOT-S aperture. The PHOT-S spectrum of IRAS04496–6958 is fainter than the CAM-CVF spectrum, whereas for IRAS05558–7000 the reverse is true. This may be a result of variability, as seen from the near-IR photometry at the epochs of these ISO observations.

References

- Ábrahám P., Acosta-Pulido J.A., Klaas U., et al., 1997, In: Heras A.M., Leech K.J., Trams N.R., Perry M. (eds.) First ISO Workshop on Analytical Spectroscopy. ESA SP-419, p. 119
- Assendorp R., Bontekoe T.R., de Jonge A.R.W., et al., 1995, *A&AS* 110, 395
- Bessel M.S., Wood P.R., 1983, *MNRAS* 202, 31
- Blanco V.M., McCarthy M.F., Blanco B.M., 1980, *ApJ* 242, 938
- Carter B.S., 1990, *MNRAS* 242, 1
- Catchpole R.M., Whitelock P.A., 1985, In: Jaschek M., Keenan P.C. (eds.) *Cool Stars with an Excess of Heavy Elements*. Reidel, p. 19
- Cesarsky C.J., Abergel A., Agnès P., et al., 1996, *A&A* 315, L32
- Dachs J., 1972, *A&A* 18, 271
- Eggen O.J., 1971, *ApJ* 163, 313
- Elias J.H., Frogel J.A., Humphreys R.M., 1985, *ApJS* 57, 91
- Elias J.H., Frogel J.A., Schwing P.B.W., 1986, *ApJ* 302, 675
- Epchtein N., Le Bertre T., Lépine J.R.D., et al., 1987, *A&AS* 71, 39
- Feast M.W., Catchpole R.M., Carter B.S., Roberts G., 1980, *MNRAS* 193, 377
- Gabriel C., Acosta-Pulido J., Heinrichsen I., Morris H., Tai W.-M., 1997, In: Hunt G., Payne H.E. (eds.) *Astronomical Data Analysis Software and Systems VI*, ASP Conf. Ser. Vol. 125, p. 108
- Glass I.S., 1979, *MNRAS* 186, 317
- Groenewegen M.A.T., Smith C.H., Wood P.R., Omont A., Fujiyoshi T., 1995, *ApJ* 449, L119
- Groenewegen M.A.T., Blommaert J.A.D.L., 1998, *A&A* 332, 25
- Hodge P.W., Wright F.W., 1969, *ApJS* 17, 467
- Hughes S.M.G., 1989, *AJ* 97, 1634
- Hughes S.M.G., Wood P.R., 1990, *AJ* 99, 784
- Hughes S.M.G., Wood P.R., Reid N., 1991, *AJ* 101, 1304
- Humphreys R.M., 1979, *ApJS* 39, 389
- Kessler M.F., Steinz J.A., Anderegg M.E., et al., 1996, *A&A* 315, L27
- Laureijs R.J., Klaas U., Richards P.J., Schulz B., 1998, *ISOPHOT Data Users Manual V4.0*. SAI/95-220/Doc
- Le Bertre T., Epchtein N., Guglielmo F., Le Sidaner P., 1994, *Ap&SS* 217, 105
- Lemke D., Klaas U., Abolins J., et al., 1996, *A&A* 315, L64
- Loup C., Zijlstra A.A., Waters L.B.F.M., Groenewegen M.A.T., 1997, *A&AS* 125, 419 (Paper I)
- Meaburn J., 1980, *MNRAS* 192, 365
- Merrill K.M., Stein W.A., 1976a, *PASP* 88, 285
- Merrill K.M., Stein W.A., 1976b, *PASP* 88, 294
- Merrill K.M., Stein W.A., 1976c, *PASP* 88, 874
- Neugebauer G., Habing H.J., van Duinen R., et al., 1984, *ApJ* 278, L1
- Noguchi K., Akiba M., 1986, *PASJ* 38, 811
- Noguchi K., Sun J., Wang G., 1991a, *PASJ* 43, 275
- Noguchi K., Sun J., Wang G., 1991b, *PASJ* 43, 311
- Oestreicher M.O., Schmidt-Kaler T., Wargau W., 1997, *MNRAS* 289, 729
- Ott S., Abergel A., Altieri B., et al., 1997, In: Hunt G., Payne H.E. (eds.) *Astronomical Data Analysis Software and Systems VI*, ASP Conf. Ser. Vol. 125, p. 34
- Payne-Gaposchkin C.H., 1971, *Smithsonian Contrib. Astrophys.* 13, 1
- Prévot L., Andersen J., Ardeberg A., et al., 1985, *A&AS* 62, 23
- Rebeiro E., Martin N., Mianes P., et al., 1983, *A&AS* 51, 277
- Reid N., 1989, *Ap&SS* 156, 73
- Reid N., Glass I.S., Catchpole R.M., 1988, *MNRAS* 232, 53
- Reid N., Tinney C., Mould J., 1990, *ApJ* 348, 98
- Ritossa C., García-Berro E., Iben I., 1996, *ApJ* 460, 489
- Roche P.F., Aitken D.K., Smith C.H., 1993, *MNRAS* 262, 301
- Sandage A., Tammann G.A., 1974, *ApJ* 191, 603
- Sanduleak N., Philip A.G.D., 1977, *Publ. Warner & Swasey Obs.* 2, 105
- Schwing P.B.W., Israel F.P., 1990, *A catalog of IRAS sources in the Magellanic Clouds*. Kluwer, Dordrecht
- Siebenmorgen R., Starck J.-L., Sauvage M., et al., 1998, *ISOPHOT Data Users Manual V4.0*. SAI/95-220/Doc
- Trams N.R., van Loon J.Th., Zijlstra A.A., et al., 1999, *A&A* 344, L17
- van der Veen W.E.C.J., Habing H.J., 1988, *A&A* 194, 125
- van Loon J.Th., Zijlstra A.A., Bujarrabal V., Nyman L.-Å., 1996, *A&A* 306, L29
- van Loon J.Th., Zijlstra A.A., Whitelock P.A., et al., 1997, *A&A* 325, 585 (Paper III)
- van Loon J.Th., Zijlstra A.A., Whitelock P.A.W., et al., 1998a, *A&A* 329, 169 (Paper IV)
- van Loon J.Th., te Lintel Hekkert P., Bujarrabal V., Zijlstra A.A., Nyman L.-Å., 1998b, *A&A* 337, 141
- van Loon J.Th., Zijlstra A.A., Groenewegen M.A.T., 1999, *A&A* in press
- Westerlund B.E., Olander N., Hedin B., 1981, *A&AS* 43, 267
- Wood P.R., 1998, *A&A* 338, 592
- Wood P.R., Bessell M.S., Fox M.W., 1983, *ApJ* 272, 99
- Wood P.R., Bessell M.S., Paltoglou G., 1985, *ApJ* 290, 477
- Wood P.R., Bessell M.S., Whiteoak J.B., 1986, *ApJ* 306, L81
- Wood P.R., Whiteoak J.B., Hughes S.M.G., et al., 1992, *ApJ* 397, 552
- Wright F.W., Hodge P.W., 1971, *AJ* 76, 1003
- Zijlstra A.A., Loup C., Waters L.B.F.M., et al., 1996, *MNRAS* 279, 32 (Paper II)